Sensors & Diagnostics

ROYAL SOCIETY OF CHEMISTRY

CRITICAL REVIEW

View Article Online
View Journal | View Issue

Check for updates

Cite this: *Sens. Diagn.*, 2024, **3**, 1369

Recent advances of optical fiber biosensors based on surface plasmon resonance: sensing principles, structures, and prospects

Jingwei Lv,[a] Jianxin Wang,[a] Lin Yang,[a] Wei Liu,[a] Haihao Fu,[a]
Paul K. Chu[b] and Chao Liu*[a]

Received 8th February 2024,
Accepted 30th May 2024

DOI: 10.1039/d4sd00045e

rsc.li/sensors

Optical fiber biosensors based on the surface plasmon resonance (SPR) phenomenon are generating increasing interest due to their capability of real-time monitoring of analytes in a biocompatible, label-free, stable, and cost-effective manner. In fact, SPR optical fiber biosensors are becoming very popular in environmental science, clinical diagnosis, disease detection, and food safety. This review provides a comprehensive overview of optical fiber biosensors that utilize SPR. The principles and recent developments of optical fiber sensors are described. Different SPR optical fiber biosensors, including traditional optical fiber SPR biosensors, microstructured optical fiber (MOF) biosensors, grating-assisted plasmon fiber SPR biosensors, and others, are reviewed and the capabilities of common biosensors are compared. This overview aims to provide guidance for future research and development of this important and burgeoning field.

1. Introduction

The surface plasmon resonance (SPR) biosensor, which is the most commonly used biosensor, has been widely utilized for monitoring interactions such as DNA and protein, antigen–antibody, and drug–protein.[1] SPR biosensors play a critical role in label-free biosensors, attributed to their high sensitivity to changes in refractive index (RI) and biomolecular behavior within the electromagnetic field near a sensing surface.[2] This optical properties of SPR have been utilized in a wide range of research areas, including optoelectronics, nanophotonics, and biochemistry.[3] Various SPR biosensors are gaining considerable attention and have rapidly taken over the sensing market because of their advantages of high sensitivity, real-time response, and being label-free.

Recently, optical fiber sensing technology has gained attention in biosensing due to distinctive features such as high sensitivity, fast detection speed, non-destructive detection, and immunity to electromagnetic interference.[4] Optical fiber biosensors typically utilize sensing and biorecognition elements to achieve biological detection.[5–7] They have diverse structures, including unclad and etched fibers,[8,9] tapered and polished fibers,[10,11] D-type fibers,[12–14] photonic crystal fibers,[15–17] fiber Bragg gratings (FBGs),[18,19] and so on. Sensing is accomplished by generating a signal related to the analyte, for instance, refractive index (RI), intensity, amplitude, and phase.[20,21] The biorecognition elements, which are the key components, are usually antigens, antibodies, enzymes, microorganisms, nucleic acids, and whole cells, which can recognize and bind to target molecules with high sensitivity and specificity.[22–25] As a specific type of optical sensor, plasmonic sensors boast high sensitivity and multiplexing capacity while not requiring expensive equipment. Therefore, several types of plasmonic sensors based on (localized) surface plasmon resonance (LSPR, SPR),[26,27] long-range surface plasmon polariton (LRSPP),[28,29] and surface-enhanced Raman scattering (SERS)[30,31] have been developed. Among them, optical fiber biosensors based on SPR are particularly attractive due to their large commercial potential in chemistry, life sciences, and other fields.[32,33]

There have been a number of studies on SPR fiber biosensors.[34–36] Fiber-optic SPR sensors, created using various post-processing techniques, combine the miniaturization and interference resistance of optical fibers with the high sensitivity and specificity of SPR technology. These sensors are applied in areas such as protein–protein,[37,38] protein–DNA,[39–41] and protein–small molecule drug[42,43] interactions, clinical biomarker monitoring, and microorganism detection. For example, Zhang *et al.* have designed an SPR biosensor to detect DNA hybridization. The

---

[a] *School of Physics and Electronic Engineering, Northeast Petroleum University, Daqing 163318, P.R. China. E-mail: msm-liu@126.com, liuchao@nepu.edu.cn*
[b] *Department of Physics, Department of Materials Science & Engineering, and Department of Biomedical Engineering, City University of Hong Kong, Tat Chee Avenue, Kowloon, Hong Kong, China*

biosensor consists of a graphene/gold film (G/Au) on a D-shape plastic optical fiber (D-POF).[44] Luo *et al.* have coated Au nanoparticles on Staphylococcal protein A to augment the affinity of anti-NDV monoclonal antibodies toward NDV.[45] Lee *et al.* have proposed an LSPR biosensor prepared by side polishing and coating with ochratoxin A (OTA) aptamer, which is capable of detecting OTA with a low detection limit and high selectivity.[46] The integration of SPR with optical fiber sensing has spurred the development of biosensing. In spite of their unique merits, optical fiber-based biosensors are still not widely accepted commercially due to some practical obstacles. Fortunately, recent advancements in optical fiber biosensors have overcome some of these constraints rendering the technology practical and competitive.

In this review, we first summarize the recent progress of optical fiber-based SPR biosensors as illustrated in Fig. 1. The sensing principles of optical fiber-based SPR sensors are introduced, and different optical fiber-based SPR biosensors are described. Finally, the present challenges and prospects are discussed.

2. Principle of SPR biosensors

Traditional SPR sensors are designed based on the prismatic structures, *i.e.*, Otto configuration and Kretschmann configuration.[47,48] The Kretschmann configuration is more versatile due to its ease of fabrication, which is achieved by directly applying the metal to the prism surface. Modification of the bioreceptors on the metallic surface is an essential requirement for biosensors that are engineered to monitor one or more components. Various proteins, cells, or microorganisms that exist in a liquid bind to the receptors as target analytes, causing variations in the refractive index of

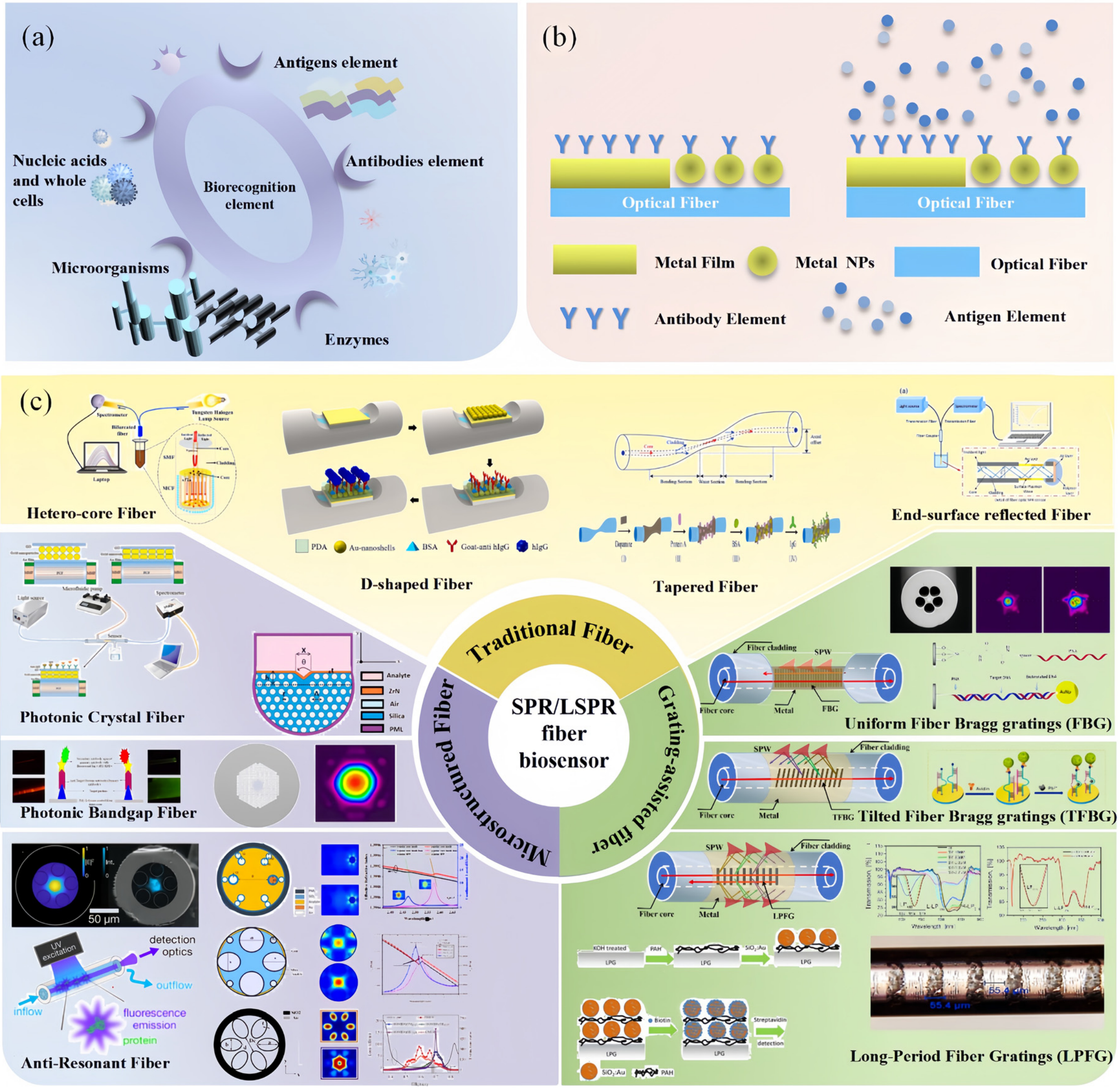

Fig. 1 Overview of optical fiber-based SPR biosensors. (a) Biorecognition elements, (b) optical fiber sensing mechanism, and (c) different optical fiber-based SPR biosensors.

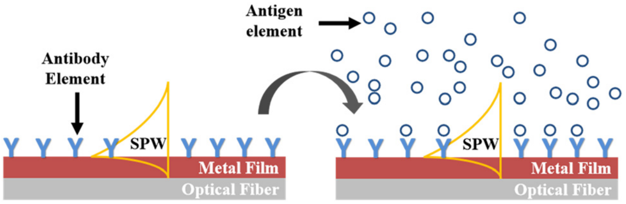

Fig. 2 Principle of SPR biosensing.

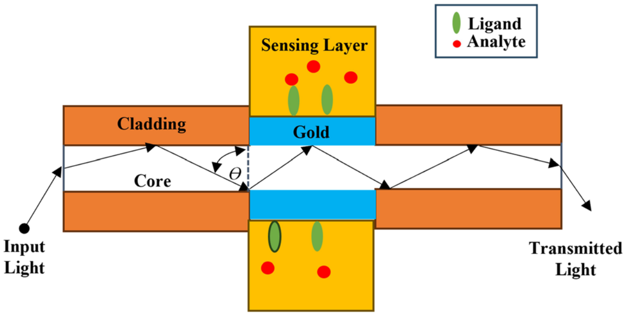

Fig. 3 Schematic diagram showing the interactions between the plasmonic optical fiber biosensor and external analyte.

the metal surface. This variation is determined by the concentration of the analyte molecules on the sensor surface and the nature of the molecules. Fig. 2 provides a summary of the antibody–antigen binding detection mechanism by the SPR biosensor.

When light diffuses to the boundary between the prism and metal, the evanescent wave (EW) generated by the incident light at the prism–metal interface excites the surface plasmon wave (SPW) at the metal–dielectric interface.[49] Owing to the gradual attenuation of the SPW propagating along the interface, the light intensity at the resonance angle or the resonance wavelength position corresponding to the matched wavevector in the total reflected light increases significantly. This phenomenon leads to the appearance of SPR resonance peaks in the reflection spectrum. The SPW propagating at the interface of a dielectric film and metal film has a propagation constant (k_{sp}) that can be defined as:[50]

$$k_{\text{sp}} = \frac{\omega}{c}\sqrt{\frac{\varepsilon_{\text{m}}\varepsilon_{\text{s}}}{\varepsilon_{\text{m}}+\varepsilon_{\text{s}}}} = \frac{\omega}{c}\sqrt{\frac{\varepsilon_{\text{m}}{n_{\text{s}}}^2}{\varepsilon_{\text{m}}+{n_{\text{s}}}^2}} \quad (1)$$

where ε_{m} and n_{s} are the dielectric constant of the metal ($\varepsilon_{\text{m}} = \varepsilon_{\text{mr}} + i\varepsilon_{\text{mi}}$) and refractive index of the dielectric materials, respectively. As indicated by eqn (1), the SPW is supported by the structure provided that $\varepsilon_{\text{mr}} < -{n_{\text{s}}}^2$. Given that the majority of the SPW field is concentrated in the medium, the propagation constant of the SPW exhibits high sensitivity to alterations in the refractive index of the medium. Therefore, highly sensitive biomolecular monitoring can be accomplished by measuring the resonance wavelength, resonance angle, or phase of the reflected beam. More details of the SPR sensing principles can be found in the literature.[50,51]

In 1993, Jorgensen *et al.* introduced the concept of optical fiber SPR sensing.[52] By removing a part of the fiber cladding, the SPR effect is observed by depositing a gold coating onto the surface of the bare fiber core with silica normally being the bulk material. Since then, various fibre post-processing techniques including bending, polishing, etching, taper stretching, periodic gratings and MOFs have been developed over the last 30 years to improve the performance of fibre optic SPR biosensors. The fundamental optical fiber sensor comprises a light source, sensing element, and spectrometer. Similar to prismatic SPR sensors, the design of the optical fiber sensing element must allow a portion of light in the fiber core to leak to the metal surface to couple with the plasmonic modes, as shown in Fig. 3. Changes in RI monitored by the sensor are translated into changes in analyte concentration by analysing the LOSS spectrum. This is followed by a review of multiple classes of fiber optic sensors, including a comparison of table-based designs and response characteristics.

3. Overview of SPR/LSPR fiber biosensors

3.1 Traditional optical fiber biosensors based on SPR

Although a lot of work has been done to design and simulate microfibers and excellent sensing properties have been demonstrated, only sensors based on the common single-mode and multi-mode fibers are usually used in experimental measurement because of their low cost, simple manufacturing process, and stable characteristics. In metal-coated fibers, SPR occurs when a part of the light transmitted in the fiber core leaks into the fiber cladding. Therefore, the fiber is partially removed from the fiber cladding and subsequently coated with metal films in order to fabricate the sensors. As the most common plasmonic materials, gold and silver are widely used in optical fiber sensors due to their relative inertness. In 2016, Ravi Kant *et al.* presented a fiber optic biosensor with a silver film for the detection of uric acid in aqueous samples.[53] The sensor is made of a large core diameter multimode fiber with the plastic cladding removed, and can be used to directly excite the SPR of silver films while maintaining a certain structural strength. Sensing depends on the effective refractive index of the sensing layer, which is modified by the enzyme complex in the enzymatic reaction. The SPR spectra of uric acid with different concentrations from 0–0.9 mM shown in Fig. 4(a) show different resonance wavelength shifts as shown in Fig. 4(b). Biosensors utilize not only a single layer, but also incorporate multiple sensing materials. For example, Pathak *et al.* have reported the SPR-based CTAB functionalized ZnO/CNTs nanocomposite and silver-coated optical fiber catechol sensor with enhanced catalytic activity in redox reactions.[54] The schematic showing the experimental set-up and synthesis of functionalized CNTs and ZnO nanoparticles and attachment of ZnO nanoparticles to CNTs walls is depicted in Fig. 4(c). A

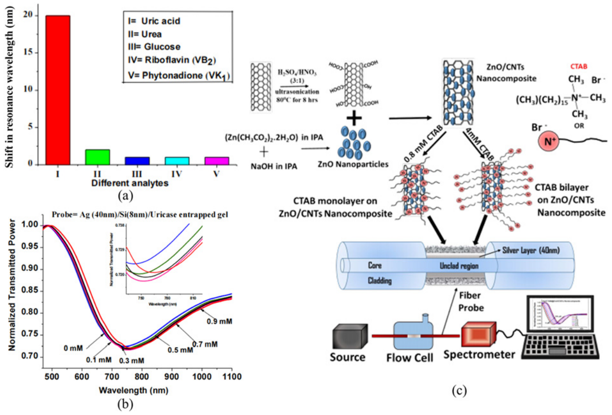

Fig. 4 (a) Shifts in the resonance wavelength for different analytes; (b) experimental SPR spectra for the optical fiber SPR probe for uric acid; (c) schematic showing the synthesis of functionalized CNTs and ZnO nanoparticles, attachment of ZnO nanoparticles to CNTs walls, CTAB functionalization of the ZnO/CNTs nanocomposite for two concentrations, fiber probe and experimental set-up.

flow cell is utilized as the inlet/outlet of the solutions inserted successively with different catechol concentrations. Polychromatic light was launched from one end of the probe and the SPR spectrum was collected by the spectrometer on the other end. ZnO/CNTs nanocomposites act as a high refractive index material in the same way as the silicon layer, enhancing the electric field penetration depth of the SPR, and a highly sensitive, portable, non-enzymatic plasma sensor has been obtained based on the same fibre optic structure as in the literature.

An optical fiber SPR immunosensor functionalized with MoS_2 nanosheets has been proposed for the detection of *Escherichia coli* (*E. coli*) down to 94 CFU mL^{-1} by Kaushik *et al.*, as shown in Fig. 5(a).[55] Polychromatic unpolarized light is used as a light source, and the dark and blank reference readings are noted to eliminate noise. Fig. 5(b) shows the UV-vis absorption spectra of the exfoliated MoS_2 nanosheets to provide complementary information on the different vibration transitions and vibrational bands. As shown in Fig. 5(c), 2D contact-mode atomic force microscopy (AFM) is employed to determine the MoS_2 nanosheet thickness and homogeneity. Graphene is frequently used to enhance the sensing properties due to its optical transparency, low resistance, high carrier mobility, and tunability.[56] Hossain *et al.* have proposed a graphene-coated optical fiber SPR biosensor for breast cancer biomarker detection, and the sensing properties with and without graphene are compared.[57] Both experimental results show that the high refractive index of the functionalized nanosheets can increase the electric field strength of SPR and improve the refractive index sensitivity of the sensors, and that the large surface area can increase the binding density of antibodies and improve the specific recognition ability. However, the fabrication process and cost of 2D materials limit the large-scale application of this type of SPR sensor.

Wei Peng *et al.* used block copolymer (BCP)-templated AuNR membranes on the surface of optical fibres to prepare LSPR biosensors for highly sensitive IgG antigen–antibody detection, as shown in Fig. 6(a).[58] Fig. 6(b) and (c) demonstrate the ability of different aspect ratios of AuNRs for antigen–antibody detection with excellent spectral characteristics, higher RI sensitivity and lower biosensing LOD compared to PS-b-PAA templated CTAB-AuNR membranes. In addition, the different aspect ratios brought about the ability to vary the detection range, and the LSPR sensing wavelength can be 650 to 900 nm, which is

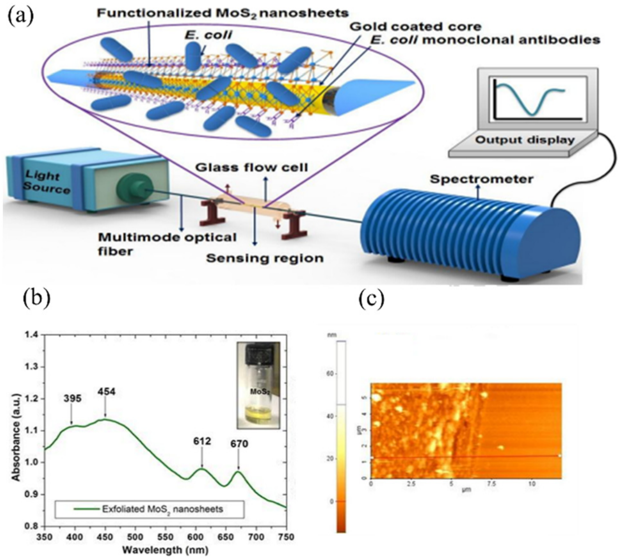

Fig. 5 (a) Schematic of the experimental setup of the optical fiber SPR immunosensor for the detection of *E. coli*; (b) UV-vis absorption spectra of exfoliated MoS_2 nanosheets; (c) 2D contact mode AFM image of the MoS_2 nanosheets and the line scan.

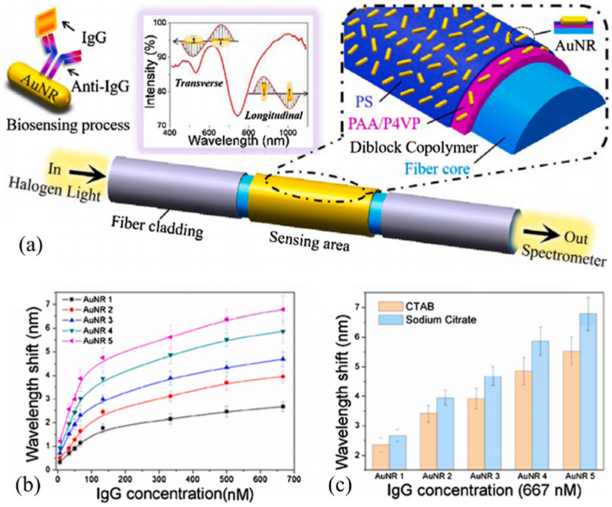

Fig. 6 (a) Schematic diagram of the AuNR-coated LSPR optical fiber biosensor; (b) calibration curve of the LSPR peak wavelength change for different concentrations of human IgG; (c) peak wavelength shift at a human IgG concentration of 667 nM.

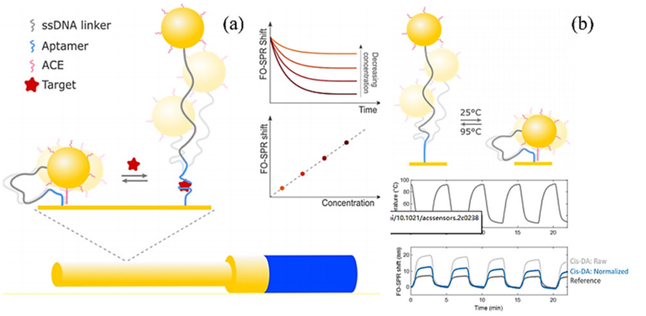

Fig. 7 (a) Schematic representation of the proposed bioassay, where *cis*-DAs are implemented on a FO-SPR sensor; (b) schematic representation of the switching between the "distal" and "proximal" state of *cis*-DA, induced by temperature cycles between 95 and 25 °C.

promising for applications in real-time biosensing without cytotoxicity.

In 2023, Dillen *et al.* reported a very interesting work on *cis*-duplexed aptamers (DAs) realised on FO-SPR sensors, where spatial position reconstruction of Au-NPs occurs upon target binding, as shown in Fig. 7(a).[59] It was expected that when the resonance conditions of the surface plasmons (SPs) on the FO-SPR sensor match those on the AuNPs, the SPs will couple and generate an enhanced signal that decays with the distance between the AuNPs and the gold film on the nm scale. The results show that the sensor is capable of specific quantitative detection of ssDNA targets with a detection limit of 230 nM and high reversibility. As shown in Fig. 7(b), by placing the sensor in repeated cycles at 95 °C and 25 °C, *cis*-DAs switches between "proximal" and "distal" states over multiple cycles. This avoids the need for complex steps to obtain a reversible signal.

3.1.1 Hetero-core optical fiber biosensors based on SPR. Hetero-core sensors typically consist of single-mode fibres, multimode fibres and photonic crystal fibres, which are used to excite the SPR by directing light within the core to the surface of the cladding. A. Hosoki *et al.* have designed a hetero-core optical fiber by inserting a segment of the single-mode fiber between two segments of the multimode fibers.[60] The sensor is constructed with multiple layers of gold (Au), tantalum pentaoxide (Ta_2O_5), and palladium (Pd), as shown in Fig. 8(a). Zhu *et al.* have proposed an optical-fiber micro-displacement sensor based on SPR by fabricating the Kretschmann configuration on the graded-index multimode fiber (GIMMF) shown in Fig. 8(b).[61] A single-mode fiber is employed to change the radial position of the incident beam as the displacement, and the displacement in the GIMMF changes the angle between the light beam and fiber axis, which is closely related to the resonance angle. As a result, the resonance wavelength of the fiber SPR shifts. The influence of temperature on the experimental results is studied and shown in Fig. 8(c). The spectrum blueshifts when the temperature rises from 20 to 50 degrees. The beam paths for different radial offsets are shown in Fig. 8(d).

Q. Wang *et al.* have fabricated an SPR immunosensor composed of graphene oxide (GO) and staphylococcal protein A (SPA) co-modified photonic crystal fibers.[62] The sensor is made by splicing a segment of the photonic crystal fiber between two segments of multimode fiber as shown in Fig. 9(a) and the detection system is depicted in Fig. 9(b). The wavelength response to human IgG at a concentration of 30 μg mL^{-1} is presented in Fig. 9(c), and the human IgG detection limit is 10 ng mL^{-1}. The sensitivities of the sensors without GO and SPA modifications were compared in the experiments, and the results showed a 30-fold difference in their detection limits.

Hetero-core optical fiber probes are used as the recognition elements in biosensing. Santosh Kumar *et al.* have proposed the MoS_2-functionalized multicore fiber probes for selective detection of Shigella bacteria.[63] As shown in Fig. 10(a), light from the tungsten-halogen source is launched at the 1st end of the bifurcated cable and coupled with the sensing probes through an adapter connected to the 2nd end of the bifurcated cable. Light interacts with the functionalized probe and the reflected light from the tip of the sensor goes to the spectrometer through the 3rd end of the bifurcated cable. The investigation of NPs is performed by measuring the dependence between the absorbance

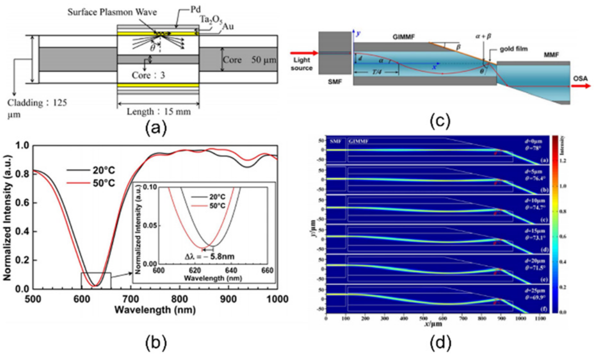

Fig. 8 (a) Micro-displacement fiber sensor and (b) micro-displacement sensor; (c) dependence of the wavelength and resonance intensity at different temperatures and (d) beam paths when the offset value *d* increases from 0 to 25 μm by simulation.

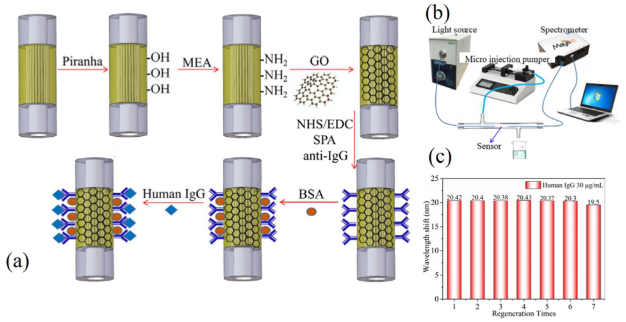

Fig. 9 (a) Graphene oxide and SPA modification of the IgG immunoassay, (b) schematic of the experimental setup of the goat anti-human IgG sensor, and (c) regeneration performance of the Au/GO-SPA immunosensor.

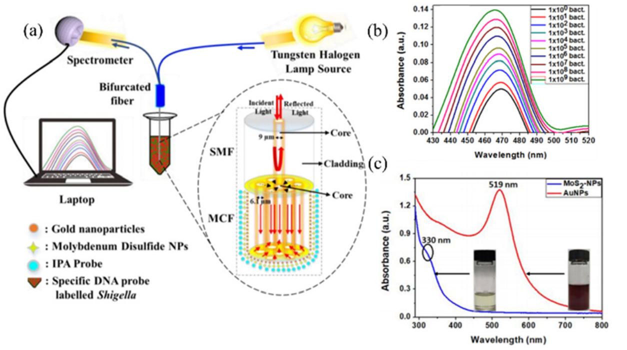

Fig. 10 (a) Experimental setup for the detection of Shigella bacteria and (b) UV-vis spectra of the AuNPs, and (c) MoS_2-NPs solutions and corresponding photographs.

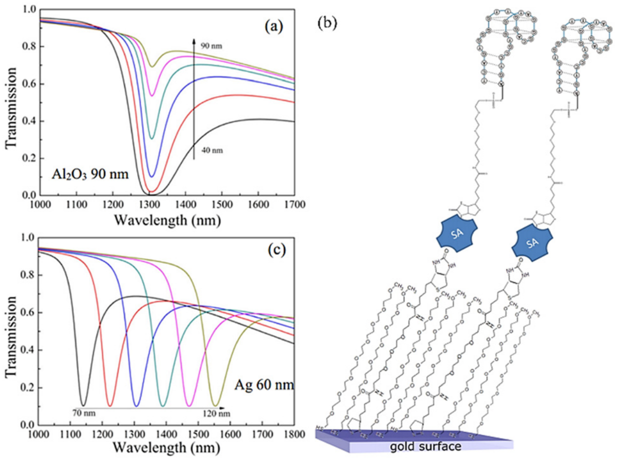

Fig. 11 (a) Transmission spectra of the SPR sensor with different Al_2O_3 thicknesses, (b) functionalization process,[66] and (c) SPR transmission spectra for different concentrations of thrombin (1–80 nM).

spectrum and wavelength, as shown in Fig. 10(b). The peak wavelengths of the synthesized AuNPs and MoS2-NPs are 519 nm and 330 nm, respectively.

The experimental results showed that multi-core fiber-optic excitation of LSPR with specific probe-modified nanostructures obtained a LOD as low as 1.56 CFU mL^{-1} against Shigella bacteria. The results show that the sensing structure of heterocore optical fibres can be improved in terms of sensitivity by increasing the polishing angle of the fibre or the refractive index of the medium, and that the partially probed sensor design is more practical for application. However, it is noted that higher processing accuracy poses limitations on further improvement of sensing sensitivity, and multiple fusion splices are not conducive to large-scale fabrication.

3.1.2 D-shape optical fiber biosensors based on SPR. The D-shape sensing structure is made by removing the partial cladding of the optical fiber along half the circumference and then coating with a thin metal film. D-shape fibers offer advantages such as a controlled evanescent field for effective sensing, a simple manufacturing process, and robustness. In 2004, Chiu proposed the first D-type single-mode optical fiber sensor as a liquid refractometer.[64] Subsequently, many D-type optical fiber sensors containing diverse sensitive materials have been suggested. Lin *et al.* have proposed a side-polished multimode fiber sensor based on SPR and performed a series of experiments.[65] The results show that the target DNA can be detected at approximately 0.1 μM on the DNA immobilized surface and the wavelength shift is 8.66 nm.

In addition to metals such as gold and silver, other materials are also used as the sensitive layers in side-polished fiber sensors. An SPR biosensor based on the D-type optical fiber coated with the $Al_2O_3/Ag/Al_2O_3$ film has been investigated numerically by Du *et al.*,[66] and the performance pertaining to gas and aqueous sensing is analyzed and compared. The transmission spectra for different Al_2O_3 thicknesses are shown in Fig. 11(a). Cennamo *et al.* have proposed a D-shape plastic optical fiber aptasensor for the detection of thrombin which is a clinical marker of the blood coagulation cascade and homeostasis,[67] as shown in Fig. 11(b). Detection can be accomplished in a short time (5–10 min) and the detection limit is about 1 nM in the range of 1.6–60 nM. The relationship between the resonance wavelength and normalized transmitted light in Fig. 11(c) shows that while THR with increasing concentration comes into contact with the nonspecific aptamer sequence, the resonance wavelength exhibits a bathochromic shift.

Xu *et al.* have presented an Au-graphene structure D-type fiber surface plasmon resonance biosensor to detect the nucleotide bonding between the double-stranded DNA helix structures.[68] To produce the structure, graphene is placed on copper. A gold layer with the optimal thickness is deposited by sputtering and the copper foil is etched to produce the structure. The transmission spectra are displayed in Fig. 12(a) and the fabrication process is illustrated in Fig. 12(b). R. Zakaria *et al.* have proposed an optical fiber

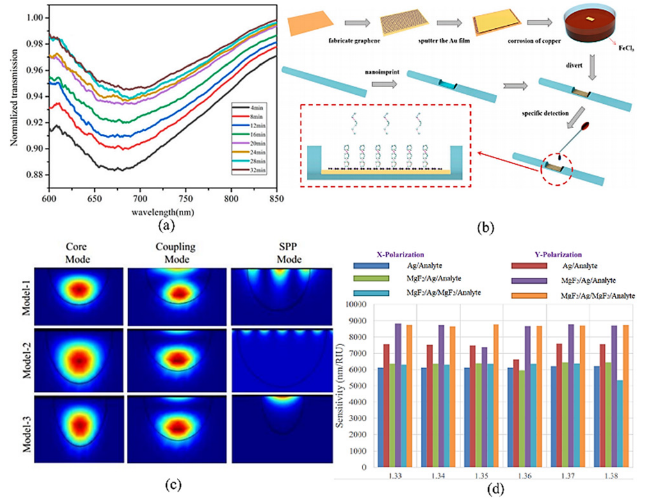

Fig. 12 (a) Transmission spectra, (b) fabrication process, (c) mode field distributions for Ag, and (d) sensitivities of the combined models.

sensor utilizing the single mode and incorporating MgF_2 as the sensing medium together with silver and gold.[69] The mode field distributions (core mode, coupling mode, and SPP mode) are shown in Fig. 12(c). The x and y polarizing sensitivities of the sensor for Ag in Fig. 10d show that they vary from 5.34×10^3 nm per RIU^{-1} to 8.34×10^3 nm per RIU^{-1} and the sensitivity in the Y direction is higher.

In addition to conventional SPR (cSPR) sensors, long-range surface plasmon resonance (LRSPR) D-type sensors deliver good sensing performance. Cheng *et al.* have proposed a side-polished fiber LRSPR biosensor with Au nanoshells to detect human immunoglobulin G (hIgG).[28] The results of Au nanoshell modification and simulation by the finite element analysis (FEA) are shown in Fig. 13(a) and (b), respectively. The study reveals that the interactions between the Au nanoshells and Au film, known as the plasmonic coupling effect, may amplify the electric field intensity on the sensor surface. This enhancement increases the sensitivity and yields lower detection limits of 1.84 nm/(μg mL^{-1}) and 0.20 μg mL^{-1}. The experimental results for hIgG detection by the LRSPR sensor and Au-nanoshell-modified LRSPR sensor are shown in Fig. 13c and d.

Compared to the heterocore structure, the D-shape fiber structure simplifies sensor fabrication and eliminates the need for complex preparation processes or special handling techniques, which reduces the experimental cost and increases the popularity of applications. Moreover, through the modification of multilayer plasma films or nanostructures, it is possible to selectively excite LSPR and LRSPR, potentially achieving both high sensitivity and low LOD for biosensing.

3.1.3 Tapered optical fiber biosensors based on SPR. Besides the aforementioned SPR biosensors, tapered optical fibers have attracted the attention of researchers. Most of the tapered fibers are made by mechanical tapering or chemical etching. Fig. 14(a) and (b) show the schematic and SEM image of the tapered optical fibers prepared by Vivek.[70] When light is transmitted to the tapered sensing region, the angle decreases gradually and approaches the critical angle of total reflection. Some of the light in the fiber core leaks out of the optical fiber to generate SPR and produce an absorption peak in the resonance transmission spectrum.

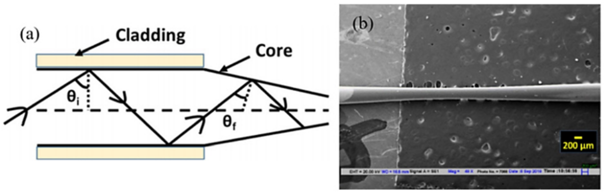

Fig. 14 (a) Schematic diagram of the tapered optical fibers and (b) SEM image of the tapered waist.

The effects of different sensing materials have been studied, and the influence of the structural parameters, such as the taper ratio and taper profile, on the sensing properties has been investigated. Many tapered optical fibers have been applied to biosensing due to the enhanced sensitivity. Cennamo *et al.* have proposed a biosensor based on MIP and SPR for the tapered plastic optical fibers in the selective and fast detection of L-nicotine.[71] The sensor can differentiate between L- and D-nicotine. The sensitivity, which is closely related to the characteristics of the tapered optical fiber, is determined by experiments. A protein sensor based on tapered optical fibers has been modified by Au coatings using two deposition methods.[72] The fibers are tapered by heating with a CO_2 laser and pulling on a rotational stage. Gold deposition proceeds by DC sputtering[73] layer-by-layer (LbL) electrostatic self-assembly as shown in Fig. 15(a). The sensitive protein biosensor can detect streptavidin below 2.5 nM and the transmission spectra for different SV concentrations are shown in Fig. 15(b).

In addition to the conventional tapered fibers, an S-tapered optical fiber biosensor has been proposed for low-concentration human IgG detection.[74] As shown in Fig. 16(a), it is bent at the taper transition, where the high-order modes are excited. A multifunctional adhesion platform is created by oxidative polymerization of the dopamine aqueous solution as shown in Fig. 16(b). The lower limit is 28 ng ml^{-1} and the influence of different stretches and axial offset lengths on the transmission characteristics of STF is studied.

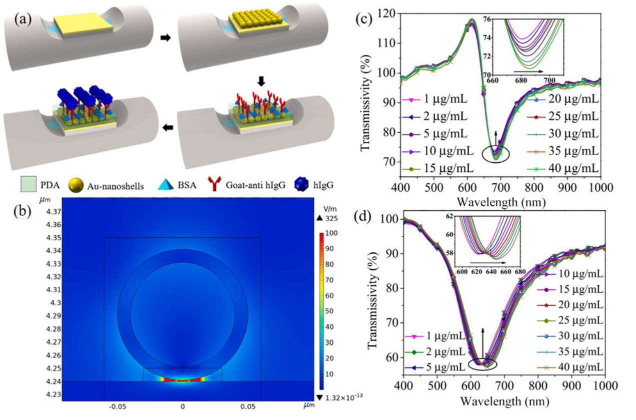

Fig. 13 (a) Au nanoshell modification, antibody immobilization, and antigen detection; (b) simulation model for the Au-nanoshell-modified LRSPR sensor; experimental results of hIgG detection: (c) LRSPR sensor and (d) Au-nanoshell-modified LRSPR sensor.

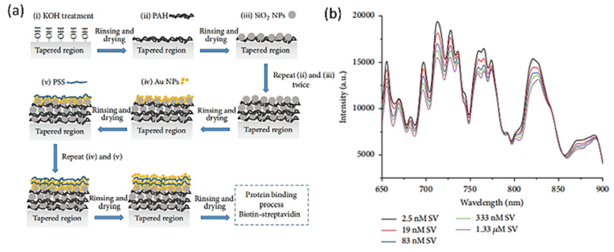

Fig. 15 (a) Schematic illustration of the coating process based on the layer-by-layer method and (b) transmission spectra for different SV concentrations.

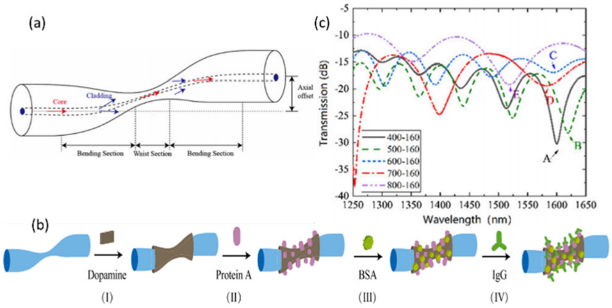

Fig. 16 (a) Schematic of the STF sensor, (b) protein A-IgG binding reaction, and (c) transmission spectra of STF.

Fig. 16(c) shows the transmission spectra of STFS for different stretch lengths and axial offsets, revealing that the number of resonant peaks and dips decreases gradually with increasing S-tapper fiber stretch length from 500 to 800 μm.

Tapered optical fibres enhance the excitation of plasma thin films by dramatically reducing the diameter of the fibre and have a very significant fabrication cost advantage, making them easier to fabricate on a large scale by mechanical tapering or chemical etching. However, the simplicity and fixed sensing structure limit the way in which the sensitivity can be increased. The fragile conical region is highly susceptible to damage, which affects the sensitivity and performance stability of the sensor.

3.1.4 End-surface reflected optical fiber biosensors based on SPR. Aside from the transmission-based optical fiber biosensor, direct insertion of an end-surface reflected sensing device into the sample simplifies detection. The end of the optical fiber is coated with a metal. When the incident light is reflected to the incident point, the optical path increases resulting in stronger resonance. Wang *et al.* have proposed a label-free optical fiber SPR biosensor for specific detection of the C-reactive protein (CRP).[75] As shown in Fig. 17(a), the end face of the sensor is deposited with an Ag reflector, and the unclad part has an Au layer deposited by magnetron sputtering. The sensor end with the Ag reflector is protected by a polymer layer as shown in Fig. 17(b). The sensor shows good linear response in the CRP concentration range from 0.01 to 20 μg ml^{-1}.

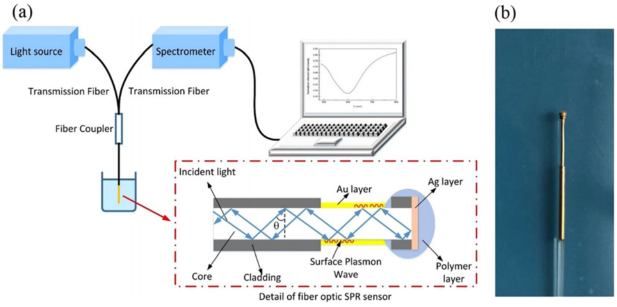

Fig. 17 (a) Schematic of the experimental setup and (b) photograph of the optical fiber SPR sensor.

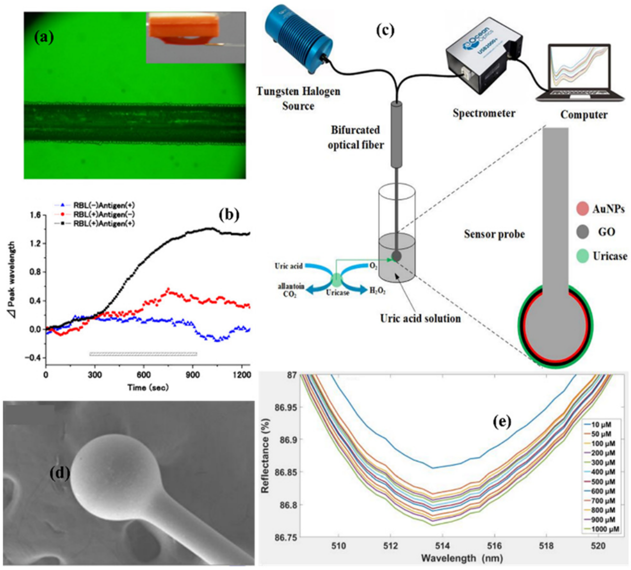

Fig. 18 (a) Image of RBL-2H3 cells fixed on the sensor tip surface; (b) dependence of the peak movement on the period of DNP–HSA perfusion; (c) experimental setup for uric acid detection by the micro-ball fiber structure; (d) SEM image; (e) variation of reflectance of solutions with different UA concentrations.

An SPR system with 250 μm diameter optical fibers has been prepared to gauge the activation of living cells.[76] The end cladding of the multimode fiber is removed with an acid and a 1 cm long gold film is deposited by vapor deposition. The RBL-2H3 cells are fixed on the sensor tip surface and observed under a phase-contrast microscope, as shown in Fig. 18(a). The dependence of peak movement on the period of DNP–HSA perfusion is shown in Fig. 18(b). The experimental results show that the peak wavelength increases for RBL-2H3 cells sensitized with anti-DNP IgE to 50 ng ml^{-1} DNP–HSA. A graphene oxide silver-coated polymer cladding formed on the silica optical fiber has been designed for SPR human IgG detection.[77] Graphene oxide enhances the confined electric field surrounding the sensing layer, and the spectral sensitivity of the sensor with graphene oxide/silver is higher than that of the silver film sensor. Santosh *et al.* have proposed a selective optical fiber-based enzymatic biosensor for the detection of uric acid (UA) in human serum.[78] Fig. 18(c) shows the experimental setup and AuNPs and GO are synthesized and characterized. The SEM image of the uricase/GO/AuNPs-immobilized micro-ball fiber is depicted in Fig. 18(d), and the reflectance plots of the uricase/AuNPs coated micro-ball fiber are shown in Fig. 18(e). Utilizing the high local electric field enhancement capability of the LSPR, the biosensor can measure different uric acid concentrations from 10 μM to 1 mM.

Sensing devices based on end-face reflection simplify the detection process for real-time biosensing, and the flexible design of the structure provides more ways to improve sensor performance. Fiber-optic end-face configurations have a significant impact on sensor performance, including planar, spherical, and prismatic configurations to modify the angle

Table 1 The characterization and sensing performance of some conventional optical SPR sensors

Ref.	Sensitive material	Sensitivity	Sensing medium	Str. Diagram
53	Ag	37 nm mM^{-1}	Uric acid	
79	Au/MoS$_2$	2.9 nm/1000 CFU mL^{-1}	*Escherichia coli*	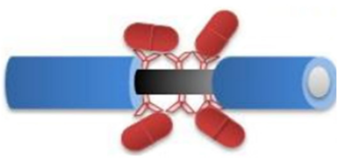
57	Au/graphene	—	Breast cancer biomarker	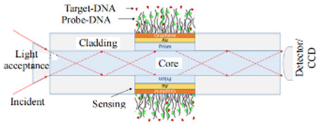
80	ITO/Cu	4583.4 (nm per RIU^{-1})	Bovine serum albumin (BSA)	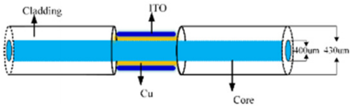
81	Graphene/Au	3030 (nm per RIU^{-1})	DNA hybridization	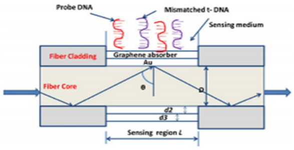
82	Ag/MoS$_2$/graphene	105.71 deg per RIU^{-1}	DNA hybridization	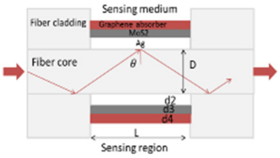
83	Cr/Au/MoSe$_2$	2793.36 nm per RIU^{-1}	Goat anti-rabbit IgG	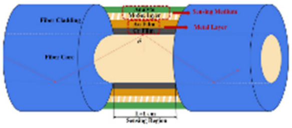
84	Au	1.857 nm UL^{-1}	Pancreatic amylase	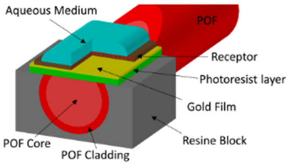
85	Ag/Ta$_2$O$_5$	8.709 nm μM^{-1} 38 nM	Acetylcholine	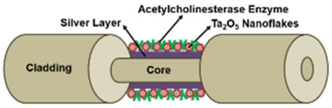
86	Au/Cr	2793.36 nm per RIU^{-1}	Prostate specific antigen	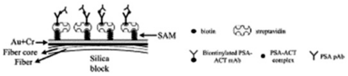
87	Ag/SnSe	3475 nm per RIU^{-1}	DNA hybridization	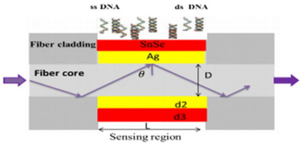
88	Ag/Al	—	Pathogenic bacteria	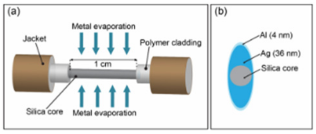
58	AuNRs	989 nm per RIU^{-1}	Antigen–antibody of IgG	

Table 1 *(continued)*

Ref.	Sensitive material	Sensitivity	Sensing medium	Str. Diagram
				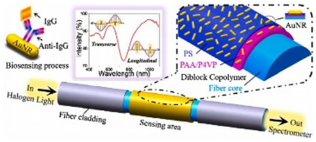

of incidence of light striking the plasma film surface. The higher fabrication complexity reduces the repeatability and stability of the sensor.

As shown in Table 1, many biosensors incorporated with metals (*e.g.*, Cr, Ni, and Al) have promising potential in DNA hybridization detection and other applications.

3.2 Microstructured optical fiber biosensors based on SPR

The microstructured optical fiber (MOF) is a novel sensing substrate that possesses a number of advantages over conventional optical fibers.[89] Specifically, the cladding area of the MOF is interspersed with a number of tiny air holes. This innovative design allows precise control of the transmission of light waves inside the core by adjusting the size and position of the air holes, as well as high intensity modulation of evanescent fields near the interface by adjusting the geometric parameters. As a result, the MOF has exceptional optical characteristics, including high sensitivity, single-mode transmission without cut-off, and adjustable chrominance dispersion.[90,91]

Microstructured optical fibers are mainly fabricated by the stack-and-draw method, as shown in Fig. 19.[92] The method typically involves assembling glass capillaries according to the desired fiber design, followed by heating and stretching the stack (filled in a clamp sleeve) to the fiber. The manufacturing process provides great flexibility in designing MOFs. In addition, the transmission mode of light waves in PCF mainly depends on the photonic bandgap effect or total internal reflection (TIR) mechanism.[93] In this way, light waves are able to propagate through the fiber core enabling precise optical control. MOFs are highly suitable for sensing applications as they offer high density, robustness, and cost-effectiveness over traditional sensors based on single-mode fibers or prisms. MOFs with their unique design and superior performance open new possibilities for optical sensing, communication, and other fields.

In SPR sensing technology, the microstructured fiber as the sensing base has structural advantages, and the flexible and controllable air holes in the cladding improve the coupling efficiency between modes. The momentum and energy matching between photons and the surface of the plasmonic medium is enhanced. Therefore, MOF-SPR sensors have attracted much attention, especially in biosensing, as the mechanism depends on the SPR effect related to the substrate and surface plasmonic materials such as Au and Ag and 2D functional materials for improved biocompatibility and molecular specific recognition (graphene, MoS_2, *etc.*).[74,94] MOF-SPR biosensors based on metal and 2D materials play a key role in medical diagnostics and body fluid detection such as cancer cell screening, DNA detection, enzymatic reactions, and identification of protein and glucose molecules.[95–97]

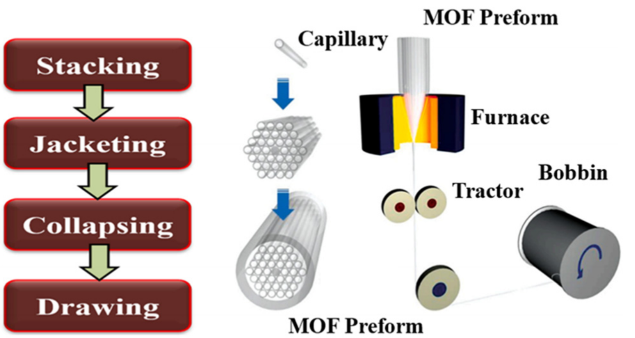

Fig. 19 Fabrication of MOFs by the stack-and-draw method.

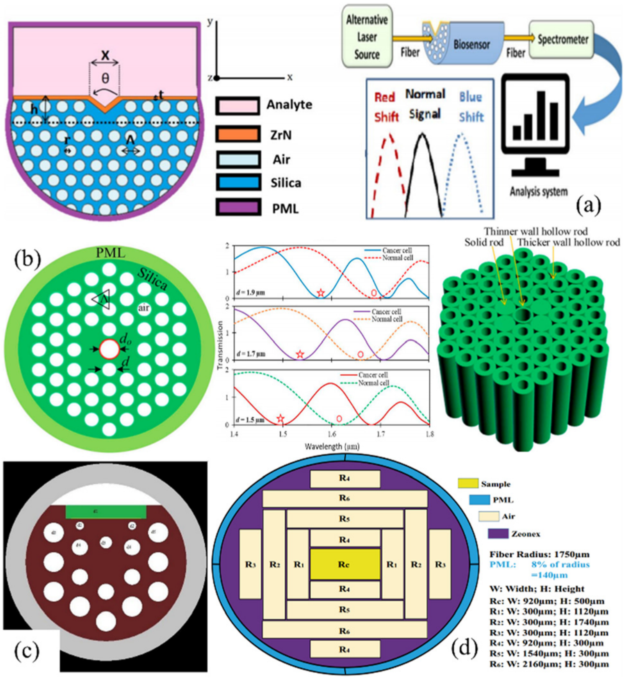

Fig. 20 Recently reported PCF biosensors for cancer detection: (a) M. Abdelghaffar *et al.*,[98] (b) Md. Aslam Mollah *et al.*,[98] (c) Mehdi fazeli *et al.*,[99] and (d) Mahmoud M. A. Eid *et al.*[100]

Currently, the primary obstacle in the advancement of optical fiber SPR sensors is the need to integrate and miniaturize devices while simultaneously enhancing the sensitivity and reliability for microscopic applications. Studies have shown that microstructured fibers have great potential.

3.2.1 Total internal reflection photonic crystal fiber biosensors based on SPR. Cancer screening and virus detection are vital to human health as they can reduce disease and reasonable screening can facilitate early intervention. M. Abdelghaffar *et al.* have proposed an SPR sensor based on PCF for the early detection of breast, basal, and cervical cancer. The PCF has a V-shape surface coated with ZrN as the plasmonic medium as shown in Fig. 20(a).[98] The coupling between the core-guided mode and plasmonic mode depends on the analytes. The V-shape enhances the sensitivity and coupling. The biosensor can be fabricated by current PCF fabrication techniques with high fabrication tolerance. Leukemia, a prevalent cancer worldwide, encompasses several forms and claims the lives of thousands annually and accurate and quick diagnosis is crucial. Md. Aslam Mollah *et al.* have presented a twin-core photonic crystal fiber (TC-PCF) for early detection of blood cancer based on the refractive index (RI) of normal and cancerous blood cells, as shown in Fig. 20(b).[99] The change in the coupling length and transmitted spectra for normal and cancerous cells is analyzed by the finite element method (FEM). According to the transmitted spectrum shift, the sensor exhibits a sensitivity of 8571.43 nm per RIU^{-1}. Mehdi Fazeli *et al.* have proposed a D-shape PCF-based SPR sensor for analytes with a refractive index of 1.33 to 1.41. Gold is used to form the plasmonic layer (Fig. 20(c)).[100] This sensor has a sensitivity between 2600 and 28 921 nm per RIU^{-1} at wavelengths of 650 to 1400 nm and has the highest resolution and best FOM of 3.46×10^{-6} RIU and 222.45 RIU^{-1}, respectively. One of the benefits of this sensor is its ability to detect cancer using blood samples and the efficient and simple structure makes it a viable diagnostic tool for analytes with different refractive indexes. M. M. A. Eid *et al.* have reported efficient detection of skin cancerous cells using the PCF-based sensor which has an asymmetrical arrangement of rectangular holes, where the core region is composed of a single rectangle and Zeonex is the fiber (Fig. 20(d)).[101] The sensor shows optimal results at 2.0 THz. The sensitivities for blood cancer cells, normal cells (Jurkat), skin cancer cells, normal cells (basal), and water are 96.74, 96.56, 96.61, 96.34, and 95.69%, respectively. In recent years, the research on SPR biosensors for diseases has increased suggesting good clinical viability.

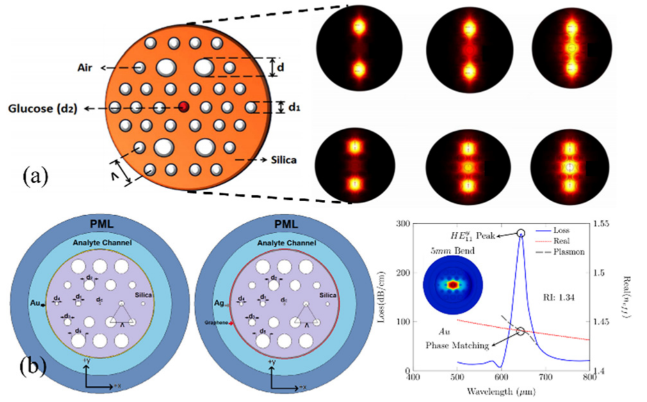

Fig. 21 SPR sensors in fluid monitoring applications: (a) Ayyanar Natesan *et al.*[102] and (b) Ahmet Yasli *et al.*[103]

The process of protein synthesis requires a large amount of energy, and glucose, the main source of energy in organisms, can also be detected by the SPR effect. Recently, PCF-SPR sensors have played a key role in human body fluid detection. Ayyanar Natesan *et al.* have proposed a glucose sensor with high sensitivity using tricore PCF that is analysed by FEM, as shown in Fig. 21(a).[102] The sensitivity is 23267.33 nm per RIU^{-1} at 470 nm of wavelength shift based on the coupling theory. Bending has an impact on the overall performance of optical fiber sensors. Ahmet Yasli *et al.* have designed an SPR biosensor based on the effects of bending (Fig. 21(b)).[103] The spectral interrogation method is chosen to calculate the sensitivity and resolution. The blood components (water, cytoplasm, blood plasma, white blood cell (WBC)) are used, and the numerical results show that the overall performance of the sensor can be improved by up to 63% by bending and the resonance wavelength can be tuned by bending.

In the process of immune regulation, the specific recognition of antigen–antibody and the interactions of biological molecules such as DNA are essential to the normal operation of living organisms. DNA determines the genetic

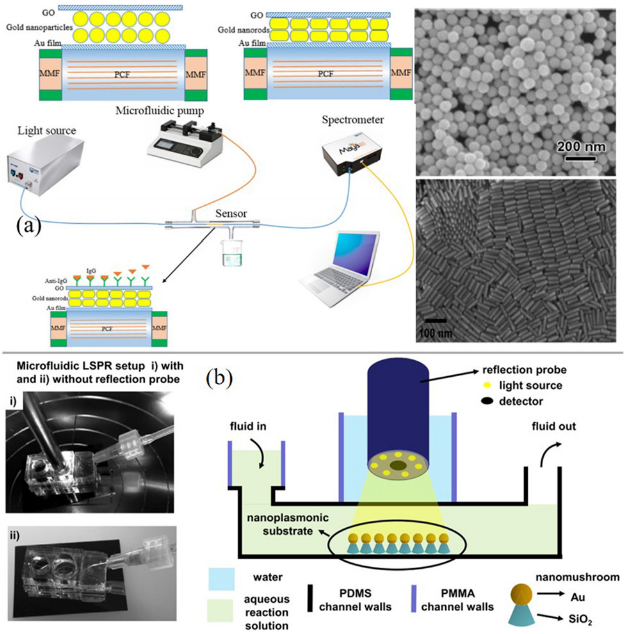

Fig. 22 Interactions of biological molecules in the immune system based on the optical fiber SPR sensor: (a) Xia *et al.*[104] and (b) J. Roether *et al.*[105]

characteristics of an organism through genetic coding and synthesises the corresponding proteins through transcription and translation. It is important to note that the SPR effect can also be used for the detection of DNA. Xia *et al.* have researched a surface plasmon resonance (SPR) fiber biosensor using multi-layer gold nanoparticles (Au NPs)/Au film to enhance the sensitivity (Fig. 22(a)).[104] The experimental results showed that SPR was able to excite the LSPR of gold nanoparticles and this coupling phenomenon between vertically aligned multilayered nanoparticles increased the depth of the outwardly propagating electric field, which induced a stronger localised electric field, obtaining a high refractive index sensitivity of 25 642 nm per RIU^{-1}. The addition of graphene oxide on the outer surface of the nanoparticles increased the number of biomolecules adsorbed and reduced the LOD to 4.6 ng mL^{-1}, which is a high sensitivity without specific modification. Deoxyribonucleic acid (DNA) is a biochemical macromolecule, which is the carrier of most biological genetic information and can provide specific biological information. The method of measuring target DNA is similar to that of the bio-immunosensor based on antibody–antigen interaction. The probe DNA is combined with the target DNA and attached to the sensor to measure the probe–target binding signal. DNA is smaller than antigens and antibodies, and sensors for the detection of DNA-related interactions require a higher sensitivity. J. Roether *et al.* have designed a microfluidic platform based on the LSPR principle for the real-time detection of DNA and polymerase reactions.[105] The platform consists of densely arranged mushroom-like nanostructures and PDMS channels (Fig. 22(b)). All the reactions are detected *in situ* inside the microfluidic LSPR chip and the sensitivity of this sensor is 54 ± 6 nm per RIU^{-1}.

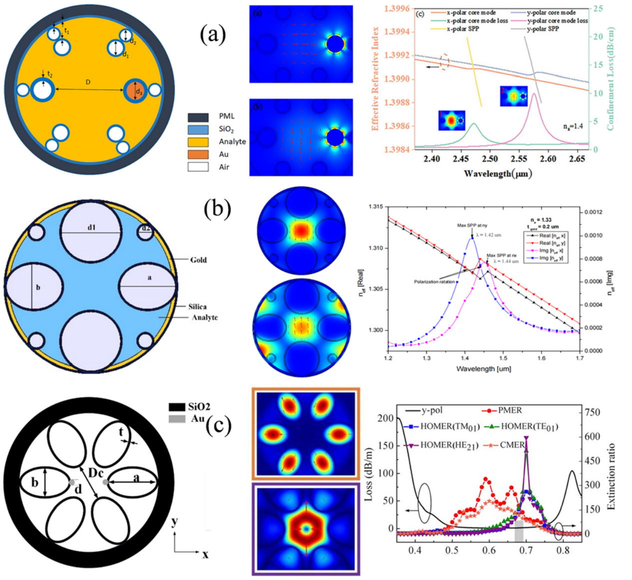

Fig. 23 (a–c) Models, light field diagrams, and curves for different ARF-SPR sensing structures.

3.2.2 Anti-resonant fiber biosensors based on SPR. Plasmonic optical fiber biosensors have garnered significant attention due to the advancement of optical fiber processing technology and increasing demand for biochemical detection, drug screening, and medical diagnostics. The anti-resonant fiber (ARF) consists of glass with a predetermined thickness.[106] The light guiding mechanism is determined by the suppression of mode coupling and the effect of anti-resonance between the cladding and core. To reduce losses and broaden the frequency band, the negative curvature tubes are used in the cladding to suppress mode coupling to a certain extent. The ARF has attracted the attention of researchers because it offers several benefits over the PBGF in terms of the simplified cladding structure, less transmission loss, and broad guiding bandwidth, which affect the detection and identification of biomolecules. Min Liu *et al.* have presented a DR-ARF sensor with a gold wire that offers high sensitivity in the detection of RI based on the SPR effect.[107] The DR-ARF consists of 12 silica tubes in two layers inside and outside, with the X-forward inner silica tube filled with the gold wire (Fig. 23(a)). The maximum sensitivity, minimum resolution, and largest birefringence of the DR-ARF sensor with the gold wire are −21 200 nm per RIU^{-1}, 4.71 × 10^{-6} RIU, and 2.38 × 10^{4} based on the birefringence analysis. The ultrahigh RI sensitivity of the DR-ARF sensor with the gold wire reveals a promising way for biochemical detection. J. Divya *et al.* have subsequently demonstrated an SPR-based hollow-core negative-curvature fiber (NCF) sensor.[108] The cladding is formed by six circular silica tubes and two elliptical silica tubes to reduce the fabrication complexity (Fig. 23(b)). The elliptical and circular silica tubes are combined to generate an anisotropic shape. The sensor can detect minor variations in the RI of the analytes placed in the hollow core. Numerical analysis by FEM in the frequency domain shows that the confinement loss is 279.69 dB cm^{-1} for *X*-polarization and 376.83 dB cm^{-1} for *Y*-polarization, in addition to FOM of 2000 RIU^{-1} for *Y*-polarization and 857.1 RIU^{-1} for *X*-polarization. Because of the simple structure, high FOM, and low transmission loss, this sensor can be used as a temperature sensor, chemical sensor, and biosensor. Wan Zhang *et al.* have designed a hollow core anti-resonance fiber based on surface plasmon resonance and optimized its characteristics using the finite element method under the perfectly matched layer boundary conditions (Fig. 23(c)).[109] A single-mode single polarization bandwidth up to 200 nm is obtained using surface plasmon resonance produced by two embedded gold wires. Only the

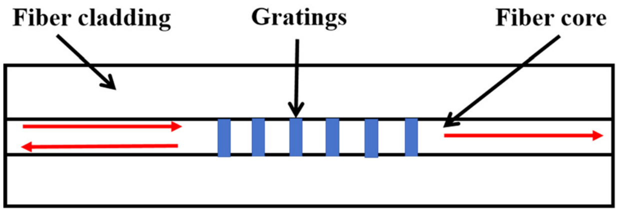

Fig. 24 Basic structure of the fiber Bragg grating.

x-polarized fundamental mode of the fiber suffers a high loss because of surface plasmon resonance. The fiber has good broadband SPSM properties in the wavelength range of 1.3 to 1.5 μm, where the extinction ratios are more than 100. Numerical simulations show that the loss difference of two polarized FMs increases because of SPR. The fiber sensor has significant promise in biochemical detection.

3.3 Grating-assisted plasmon fiber biosensors

A fiber grating is a common fiber optic device that necessitates periodic modulation of the refractive index in the core of the fiber, as shown in Fig. 24. The fiber is typically manufactured as a single mode fiber, with a 125 μm diameter cladding surrounding the 8 μm diameter core. Depending on the grating period, they are classified as long-period fiber gratings and short-period fiber gratings (grating period less than 1 μm). Conventional short-period fiber Bragg gratings (FBGs) are narrowband, wavelength-selective filters. The inverted core modes confined within the fiber core renders them insensitive to the surrounding medium. According to the well-known Bragg conditions:[110]

$$\lambda_{\text{FBG}} = 2n_{\text{core}}\Lambda \tag{2}$$

where λ_{FBG} is the resonance wavelength at which the coupling occurs, and n_{core} is the effective RI of the core mode. In order to direct some of the light inside the core to interact with the metal coating and excite plasmonic resonance, long-period fiber gratings (LPGs) or tilted fiber Bragg gratings (TFBGs) are used for the cladding modes. According to the weak waveguide approximated electromagnetic theory, the relationship between the effective refractive index of each cladding mode and its coupling wavelength can be expressed by the phase matching condition:

$$\lambda_{\text{clad}}^{i} = (n_{\text{clad}}^{i} + n_{\text{core}})\Lambda/\cos\theta \tag{3}$$

where the superscript i denotes the number of modes. Various fiber grating SPR biosensors have been developed since the integration of fiber grating and plasmonic resonance technology in 2006.[111] However, it is necessary to sort out the various fiber grating structures combined with surface plasmon sensing technology. In this section, SPR-based fiber grating biosensors are presented according to the grating cycle classification.

3.3.1 Uniform FBG biosensors based on SPR. FBGs are characterized by periodic and permanent refractive index modulation of less than 1 μm in the core of the fiber. This structure enables the fulfilment of phase matching between the fundamental core modes and backpropagation core modes. When the optical signal reaches the grating region, a part of the power is reflected, and the remainder is transmitted. The operating band of the FBG in SPR-based sensors reported in the literature is typically in the visible region (Table 2).

Due to the confinement of light within the fiber core, sensors with gold nanofilms fabricated on the cladding surface generally exhibit low sensitivity (20–74 nm per RIU^{-1}).[120,121] Post-processing, such as partial or complete removal of the cladding to expose the transmitted beam inside the fiber core to the external refractive index (including etching, grinding, and refinement of the cones), is required.

Arasu *et al.* have investigated FBG-SPR sensors with the cladding etched by performing numerical simulation.[122] Incorporation of FBG into the fiber-based SPR structure leads to a high sensitivity above 500 nm per RIU^{-1} and 4-fold increase in the signal-to-noise ratio (SNR). Burgmeier *et al.* have etched the cladding with hydrofluoric acid and modified the surface with gold nanoshell particles to excite SPR, as shown in Fig. 25.[123] The sensor which operates based on intensity modulation exhibits a high sensitivity of −4400%/RIU in the refractive index range of 1.333–1.346. Although the sensor is exclusively used in replicate experiments with anhydrous ethanol aqueous solution, the study shows the capability of FBG for biosensing. Bekmurzayeva *et al.* have reported an SPR biosensor based on etched FBG for thrombin detection.[124] The sensor with the cladding etched to 25 μm can selectively detect thrombin.

However, the post-processing approach diminishes the robustness and standardized fabrication capability of the sensor. To achieve SPR excitation without compromising the cladding structure, Chah *et al.* have fabricated gold-plated FBG sensors with biased cores using a femtosecond laser.[125] These gratings which make the fiber core highly birefringent generate a large number of cladding modes. While this approach preserves the intact cladding structure, the maximum refractive index sensitivity is limited to 50 nm per RIU^{-1}. Candiani *et al.* have proposed a DNA sensing approach based on peptide nucleic acid (PNA)-functionalized MOF Bragg gratings, as illustrated in Fig. 26.[126] The inner surface of the 'grapefruit' geometry MOF is functionalized with a PNA probe. After the penetration of the DNA solution into the fiber capillaries and hybridization, the oligonucleotide-functionalized gold nanoparticles (ON-Au NPs) are added. Spectroscopic assessment of the reflected signals reveals a significant wavelength shift of the 100 nM DNA solution in higher-order modes. The feasibility of this sensor for biomolecular measurements is demonstrated.

Arasu *et al.* have proposed an FBG sensor coated with graphene oxide and utilized gold as the plasmonic medium.[127] Experimental results show that the sensitivity is 500 nm per RIU^{-1} in the refractive index range of 1.332–1.357, which is 2.5 times higher than that of the sensor without the graphene oxide film. The FBG requiring no additional post-processing renders the sensor highly robust and easy to handle. Rusyakina *et al.* have designed additional cladding modes to excite surface plasmon resonance using FBGs fabricated based on PCF, as shown in Fig. 27.[128] The effects of PCF lattice spacing and pore diameter on the resonance spectra are discussed, and the wavelength

Table 2 The recent advances in design, application, and peculiarity of MOF biosensors

Ref.	Structural features	Detectable biochemical analytes	Performance parameters	Str. diagram
112	D-shaped titanium coated	Cancer cells	Sensitivity: 18 071.42 nm per RIU^{-1} DL: 0.025 RIU DR: 1.36–1.401 WR: 500–2000 nm	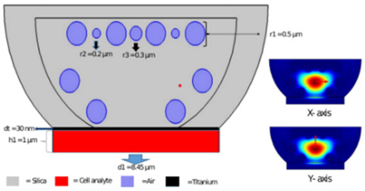
113	Circular-shaped gold and titanium dioxide coated	Blood compositions like red blood cells (RBCs), hemoglobin (HB) and white blood cells (WBCs)	Sensitivity: 12 400 nm per RIU^{-1} DL: 0.02 RIU DR: 1.33–1.40 WR: 600–1100 nm	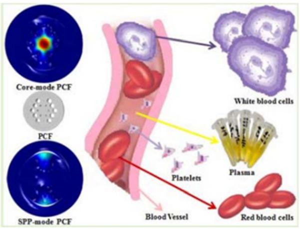
114	Circular-shaped gold coated	Malaria in human body	Sensitivity: 14 285.71 nm per RIU^{-1} DL: 0.029 RIU WR: 700–1000 nm	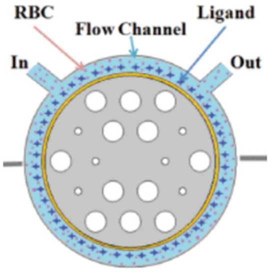
115	D-shaped Au/Ti3C2Tx MXene hybrid coated	Protein, viruses, cancer, and blood cells	Sensitivity: 13 000 nm per RIU^{-1} DR: 1.33–1.39	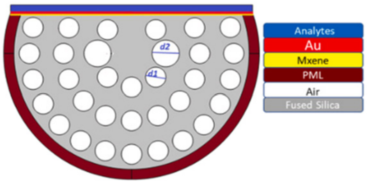
116	PBGF Alexa Fluor 700–labeled DNA Oligo	Biomolecules in ultra-small sample volumes	Volume: 1 μL LOD: 0.2 μM	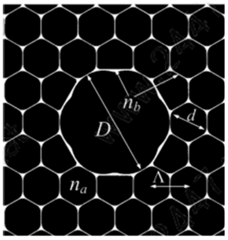
117	Circular-shaped gold coated with TiO$_2$	Biochemical sensing, medical testing	Sensitivity: 10 000 nm per RIU^{-1} Amplitude sensitivity: 1115 RIU^{-1} DR: 1.35–1.40 WR: 500–1350 nm	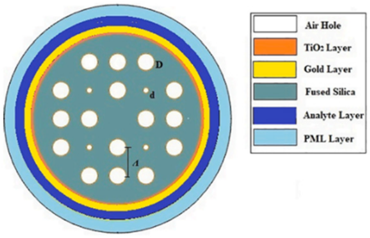
118	Convex fiber-tapered gold NPs/Nb2CTx MXene	Creatinine detection in aquaculture	Sensitivity: 6701.03 nm per RIU^{-1} DR: 1.3246–1.3634 WR: 1400–2200 nm	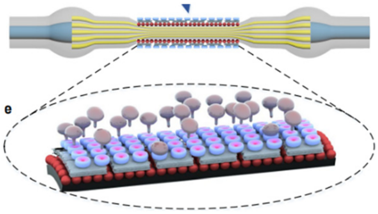

Table 2 *(continued)*

Ref.	Structural features	Detectable biochemical analytes	Performance parameters	Str. diagram
119	D-shaped silver coated with graphene and ZnO	Biochemical analytes, food quality, and medical diagnosis	Sensitivity: 4485.7 nm per RIU^{-1} DR: 1.36–1.41	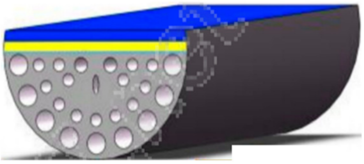

sensitivity and amplitude sensitivity of the sensor in aqueous solutions for the refractive index range of 1.3158–1.3177 are experimentally verified. Although the detection range of the sensor is limited, this study highlights the biosensing potential of FBGs based on MOF.

3.3.2 TFBG biosensors based on SPR. FBGs and TFBGs (θ < 45°) are distinguished by the difference in the angles between the gratings and fiber axis. Both gratings can excite narrow spectral bands at the so-called Bragg wavelength for reverse transmission. In TFBG, the uniform period modulation is tilted at an identical angle with respect to the fiber axis, and the modulation period is typically ~500 nm. As the effective refractive index of the cladding modes depends on the refractive index of the ambient medium, the TFBG refractive index sensors only require direct monitoring of the spectral displacement of the cladding mode resonance.[128] The refractive index detection region is in the 1.3–1.45 range, and the resulting sensitivity peaks between 10 nm per RIU^{-1} and 25 nm per RIU^{-1}. The TFBG is also capable of directing some light to the cladding–air interface to generate a swift wave that is crucial to exciting SPR.[129] When the axial component of the propagation constant of a cladding mode is equal to the SPP mode propagation constant, it experiences more losses than the neighbors. As the amplitude of certain resonances diminishes or vanishes, this phenomenon is observed from the transmission spectra of the cladding modes.[130]

Shevchenko *et al.* have designed a TFBG-assisted SPR sensor for the detection of biomolecular targets at various concentrations, as shown in Fig. 28(a).[131] The sensor shows robust detection of thrombin in serum with an SNR of 194.51 and LOD of 22.6 nM. By coating the surface with a linker protein, the TFBG-SPR sensor is capable of real-time analysis of the cellular behavior.[132,133] Voisin *et al.* have achieved a low LOD of 2 pM in the detection of streptavidin pairs.[134] Guo Tuan *et al.* have proposed the utilization of TFBG and SPR excitation for highly sensitive protein detection (sensitivity up to 5.5 dB/(mg ml^{-1}) with an LOD of 1.5 × 10^{-3} mg ml^{-1}). As shown in Fig. 28(c), by precisely controlling the thickness of the metal film to about 30 nm, some of the cladding modes can be excited by SPR using the cladding mode through the metal layer.[135] Compared with other biosensors, the sensor has the inherent temperature-sensitive property that can be eliminated by experimental processing.

Ribaut *et al.* have achieved a significant milestone by demonstrating that the TFBG-SPR sensor can accurately monitor biomarkers in biological tissues and detect cancer markers in human lung biopsies.[136] The sensor is enclosed in a specialized package made of a biocompatible polymer, which is employed as an impregnated probe for the detection

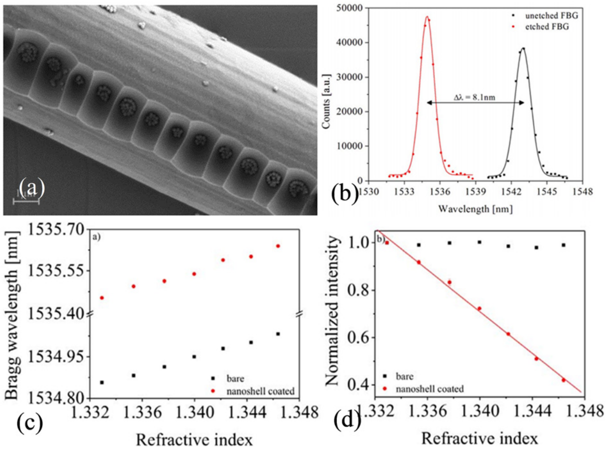

Fig. 25 (a) SEM image of etched FBG with a nanoshell coating and an increased particle density in the microstructured fiber grating area; (b) reflecting spectra of the unetched and etched FBG; SRI-dependent sensing response of the bare and nanoshell coated fiber tip: (c) Bragg wavelength and (d) amplitude.[123]

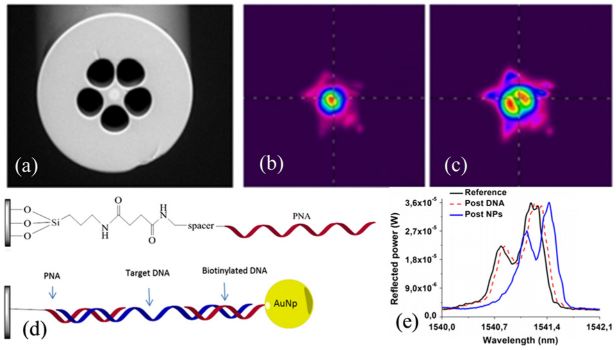

Fig. 26 (a) Scanning electron micrograph of a microstructured optical fiber (MOF); (b) basic profile and (c) first-order beam profile; (d) schematic showing the linkage of the peptide nucleic acid (PNA) probe to the fiber internal surface and sandwich-like system used for DNA detection; (e) spectra after hybridization with 100 nM full-match DNA solution and gold nanoparticles.[126]

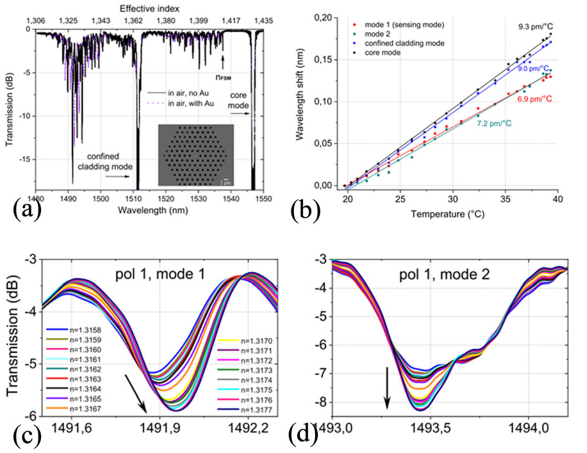

Fig. 27 (a) Transmission spectra of FBG in PCF (micrographs of cross-sections shown); (b) resonance wavelengths for the selected modes showing different dependence on the temperature variations in water; (c and d) transmission spectra of modes 1 and 2 after immersion of the gold-coated PCF gratings in solutions with 17 refractive indexes; modes showing the largest shifts in wavelength and amplitude in the SPR-excited state.[128]

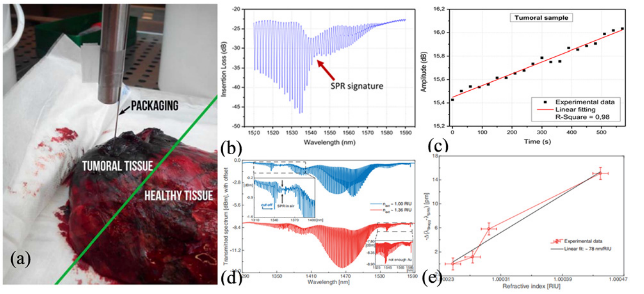

Fig. 29 (a) Picture of the immunosensor incorporated into the tumoral tissue of human lung biopsy; (b) TFBG-SPR spectrum recorded when the immunosensor is inserted in the tissue; (c) amplitude monitoring of the most sensitive mode obtained on the tumoral tissue of the biopsy;[136] (d) transmitted spectra of the TFBGs coated with a gold film 18 nm thick for SPR excitation in air;[138] (e) refractive index sensitivity of the sensors in the presence of different gases.

of cytokeratin CK17 encapsulated in an acrylamide gel matrix, as shown in Fig. 29(a). The experimental results demonstrate the existence of a stable optical response of TFBG-SPR despite the non-liquid nature of the sample. The TFBG-SPR sensor has the capability of sensitive non-invasive measurement *in situ* and online monitoring of tumors. Furthermore, Zhang *et al.* have realized online monitoring of glucose in human serum using TFBG coated with a nanoscale silver film on the surface.[137] The sensor utilizes the etching effect of hydrogen peroxide to achieve highly sensitive monitoring of glucose. A hydrogen peroxide concentration as low as 0.2 μM can be detected by monitoring the amplitude changes in selected cladding patterns. González-Vila *et al.* have performed direct sensing of different gases without the need for adaptive and sensitive coatings, as shown in Fig. 29(d).[138] The metal coating on the sensor is about one-third the thickness normally used for liquids, and the sensitivity of direct measurement of the refractive index of gases is 78 nm per RIU^{-1}.

Wang *et al.* have performed the detection of heavy lead ions (Pb^{2+}) by constructing gold nanoparticle (GNP) films on the surface of TFBG using DNAzyme and the substrate chain.[139] As Pb^{2+} cleaves the ribonucleotide adenosine linked to the DNAzyme containing the substrate strand, the GNPs linked to the DNAzyme fall onto the sensor surface, as shown in Fig. 30. The 'hot spot' effect enhances spectral signal response, enabling direct monitoring of the Pb^{2+} concentration. The experimental results show that the sensor has fine selectivity for Pb^{2+} against other environmentally relevant metal ions due to the specific recognition of DNAzyme. Qu *et al.* have fabricated an 18° TFBG-SPR biosensor for esophageal cancer diagnosis.[140] By fabricating the NY-ESO-1 antigen as a bioreceptor on a metal surface, the

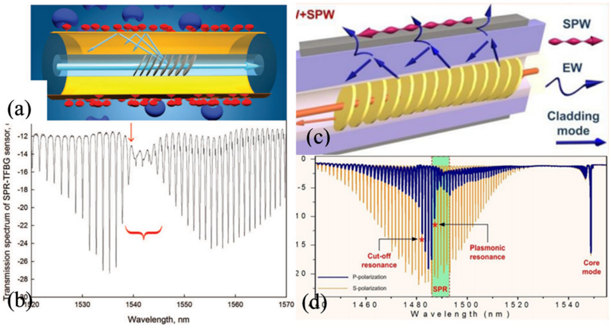

Fig. 28 (a) Monolayer of thrombin aptamer probes (shown in red) immobilized on the gold coating interacting with the cognate thrombin protein targets (shown in blue);[131] (b) sensor response measured in the aptamer solution (red arrow indicating the most sensitive SPR-coupled cladding resonance.); (c) TFBG with 20–30 nm Ag coating (hybrid "cut-off" and "plasmonic" resonances achieved simultaneously over a single TFBG);[135] (d) transmission spectra of the sensor in aqueous solutions (red stars indicating the corresponding positions of the "cutoff" and "plasmonic" resonances).

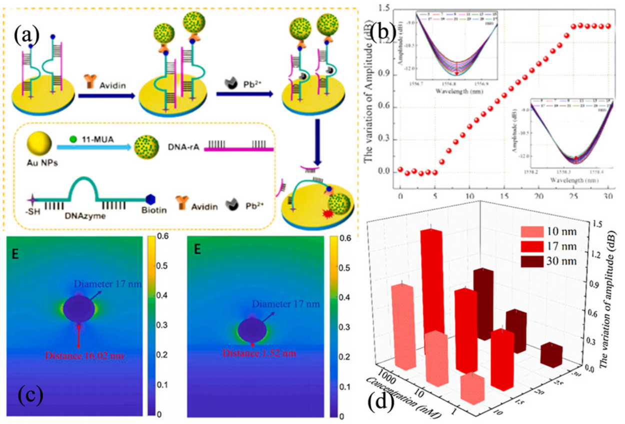

Fig. 30 (a) Schematic showing lead detection by the TFBG-SPR sensing system; (b) amplitude responses of the TFBG-SPR sensing cladding modes; (c) electric field distributions of the gold nanoparticles on the Au film with gap distances of 16.02 nm and 1.52 nm; (d) effects of gold nanoparticles with different sizes on the signals.[139]

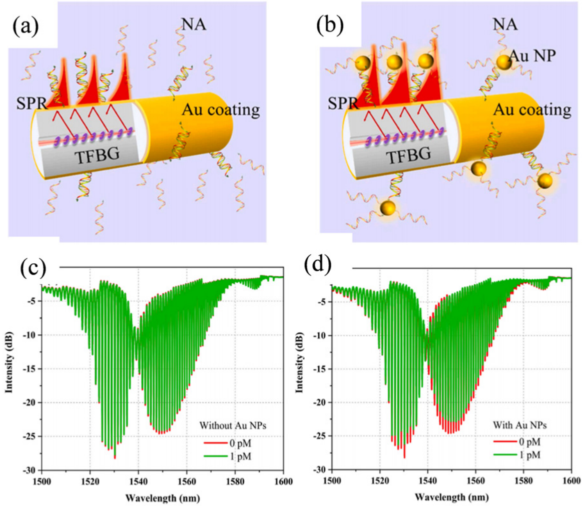

Fig. 31 Enhancement of sensitivity to NA of a TFBG-SPR sensor by using gold nanoparticles bonded onto the target NA chains. (a and b) Schematic representations of the sensing scheme (a) without and (b) with gold nanoparticles. (c and d) Transmission spectra of the sensor (c) without and (d) with gold nanoparticles.

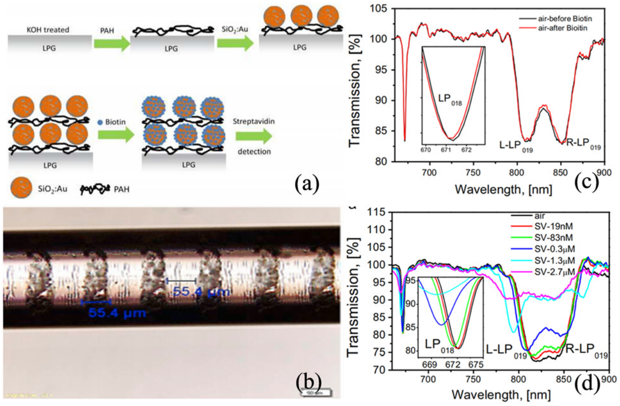

Fig. 32 (a) Schematic illustration of layer-by-layer deposition of a (PAH/SiO_2: Au)$_2$ film on the optical fiber LPG; (b) optical image of LPG; transmission spectra of LPG coated with (PAH/$SiO_{2(300\ nm)}$: Au)$_3$ exposed to (c) biotin and (d) streptavidin with different concentrations.

sensor has an LOD of 2 × 10^{-7} μg ml^{-1} with good linear monitoring of the antibody in the range of 2 × 10^{-7} to 2 × 10^{-5} μg ml^{-1}. The sensor shows the hook effect if the concentration of the NY-ESO-1 antibody is higher than 2 × 10^{-3} μg ml^{-1}.

As shown in Fig. 31(a), conventional TFBG-SPR sensors are not able to achieve effective sensing for a relatively small number of base pairs (*e.g.*, 20 base pairs to form a chain of approximately 6.8 nm long nucleic acids (NAs)).[141] In order to detect ultra-low concentrations of NAs, optical fibre sensing structures with ultra-high RI sensitivity are often required, a goal that often requires the fabrication of complex plasma structures/materials on the fibre surface. In 2023, Peng *et al.* reported a TFBG-SPR-based NA sensor with ultra-low LOD, utilising a relatively simple method to amplify RI changes, as shown in Fig. 31(b). The SPR enhancement on the Au surface was obtained by binding AuNPs to DNA strands, due to which the LSPR was excited. The TFBG-SPR NA sensor was shown to have a LOD of 1.0 × 10^{-18} mol L^{-1} (1 aM) over an ultra-wide NA detection range of 1 × 10^{-18} mol L^{-1} to 1 × 10^{-17} mol L^{-1}.

3.3.3 LPFG biosensors based on SPR. Long-period fiber gratings (LPFGs) typically have modulation periods in the range of 100 μm to 1 mm. In single-mode fibers, gratings direct light within the core into the cladding and create one or more attenuation bands in fiber transmission.[142] These cladding modes generate abrupt waves at the cladding/dielectric interface, making them inherently sensitive to surrounding refractive index (SRI) variations, resulting in significant wavelength shifts. Investigations of LPG sensors demonstrate that incorporating SPR can improve sensitivity. For example, He *et al.* have designed and analyzed an LPFG-SPR sensor by numerical simulation.[143,144] The sensor shows a resolution of −45 dB in the RI range of 1.395–1.405 besides a high sensitivity of 27 000 nm per RIU^{-1}. This forms the foundation for the future development of biosensors and chemical sensors.

Tang *et al.* have demonstrated a biosensor based on the long-period fiber grating.[145] The gold nanoparticles with a diameter of 8 nm form a self-assembled monolayer gold colloid on the grating surface, and the colloidal gold surface is modified with the dinitrophenyl compound (DNP).[146] An LOD as low as 9.5 × 10^{-10} M is achieved by measuring the transmission spectra of the sensing fiber grating. Marques *et al.* have coated SiO_2:Au NPs on the surface of LPFG for protein detection, as shown in Fig. 32.[147] The SiO_2 NPs serve two important functions. Firstly, they confer higher porosity to the sensitive layer of the sensor, thus providing a larger surface area. Secondly, they optimize the efficiency of the interactions between the swift wave and the sensitive layer by optimizing the thickness of the sensitive layer. Biotin–streptavidin is directly attached to the Au shell layer of silica NPs, and the selectivity of the sensor for specific proteins can be tailored simply by changing the nature of the ligand.

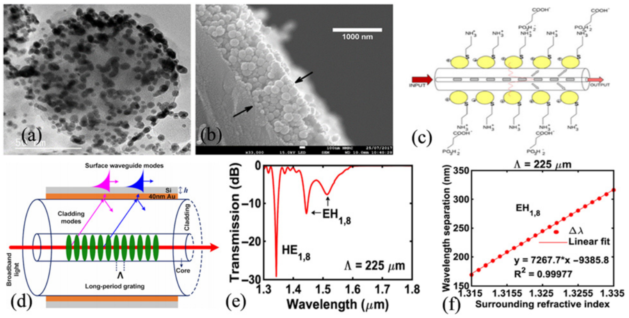

Fig. 33 (a) TEM image of SiNPs with a gold shell;[149] (b) cross-sectional image of the optical fiber with three layers of PAH/SiNPs and gold shell; (c) schematic drawing of the LPG-AuNP-Cys fiber sensor;[150] (d) LPFG coated with gold–silicon films; (e) transmission spectrum for the 225 um grating period; (f) wavelength variation and sensitivity of the $EH_{1,8}$ modes.[151]

Table 3 The characterization and sensing performance of some typical FBG-SPR sensors

Ref.	Design specifications	Analyte parameters	Performance parameters	Str. diagram
122	FBG (cladding diameters: 5.8 um) + Au(40 nm)	RI (1.33–1.44)	Sensitivity: 522 nm per RIU^{-1} (1.33–1.38)/1246.7 nm per RIU^{-1} (1.38–1.44) SNR: 0.24 (1.33–1.38)/0.46 (1.38–1.44)	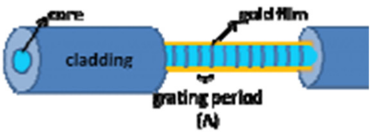
125	FBG (Eccentric) + Au(30 nm)	RI (1.33–1.36)	Sensitivity: 50 nm per RIU^{-1}	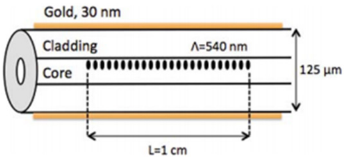
123	FBG (cladding diameters: 6um) + SiO_2:Au NPs(diameters: 155 nm)	RI (1.3329–1.3422)	Wavelength sensitivity: 13.5 nm per RIU^{-1} Amplitude sensitivity: −4400%/RIU	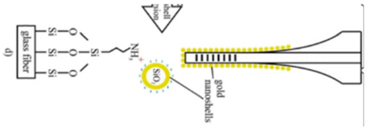
127	FBG + Au(45 nm) + GO	RI (1.345–1.3550) RI (1.3550–1.3597)	Sensitivity: 486 nm per RIU^{-1} SNR: 1.85 Sensitivity: 1340 nm per RIU^{-1} SNR:1.76	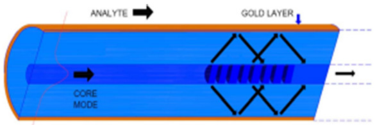
128	FBG (PCF cladding diameters: 86um, air hole diameters: 1um, ∧ = 2.5um) (∧ = 541 nm,) + Au(35 nm)	RI (1.3158–1.3177)	Wavelength sensitivity: 40.3 nm per RIU^{-1} Amplitude sensitivity: −801 dB/RIU, SNR: 1.02 × 10^{-4} RIU	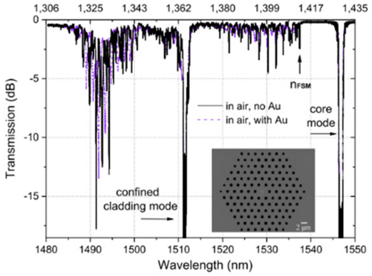
131	TFBG (θ = 10°) + Au(50 nm)	Thrombin (0–5 µM) Aptamers (0–20 µM)	SNR: 2.11–194.51 LOD: 22.6 nM SNR: 8.58–36.97 LOD: 2 nM	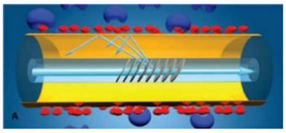
137	TFBG (θ = 18°) + Ag(30 nm)	Glucose concentrations (0–12 mM)	Sensitivity: 0.5 dB mM^{-1} LOD: 0.2 µM	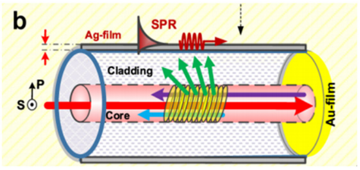
140	TFBG (θ = 18°) + Au(50 nm)	NY-ESO-1 antibody (2 × 10^{-7} − 2 × 10^{-5} µg ml^{-1})	LOD: 2 × 10^{-7} µg ml^{-1}	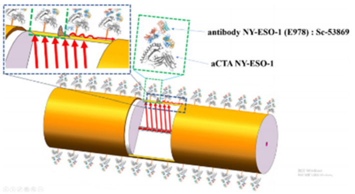
145	LPFG (∧ = 550 um) + Au NPs with an average diameter of 8.4 ± 2.8 nm	Dinitrophenyl (DNP) antibody	LOD: 1.4 × 10^{-8} g mL^{-1} or 9.5 × 10^{-10} M	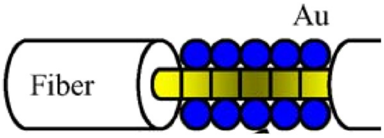
144	LPFG (∧ = 47.57399 um, number of periods N = 39) + Au film	Analyte refractive index from 1.395 to 1.405	Sensitivity = 27 000 nm per RIU^{-1}	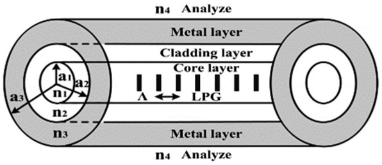

Table 3 *(continued)*

Ref.	Design specifications	Analyte parameters	Performance parameters	Str. diagram
148	LPFG ($\wedge$ = 600um)(cladding diameter of 125 μm) + Ag(50 nm) + graphene	0–3.5% methane gas	Sensitivity = 0.344 nm%$^{-1}$	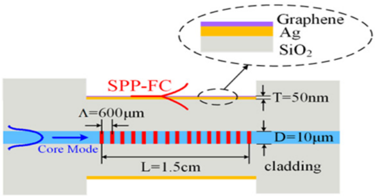
151	LPFG ($\wedge$ = 225um) + Au(40 nm) + Si(45.5 nm)	Around 1.315 RIU	Sensitivity = 7267.7 nm per RIU^{-1}	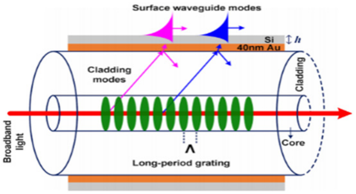

Streptavidin can be detected at a minimum concentration of 2.5 nM, with a sensitivity of 6.9 nm (ng mm^{-2})$^{-1}$ and a detection limit of 19 pg mm^{-2}. Subsequently, Wei *et al.* have increased the strength of the surface electric field by coating a layer of graphene on the surface of the Ag membrane of the LPFG-SPR sensor.[148] The experimental results show that the interactions between the SPR wave and the molecule are significantly enhanced, and the sensitivity of the sensor for methane reaches 0.344 nm%$^{-1}$, which is 1.31 times higher than that of the conventional LPFG-SPR sensor.

Liu *et al.* have adopted a similar approach in preparing SiO_2:Au NPs on LPFG by a layered method, as shown in Fig. 33(a).[149] The Au NPs (2–5 nm in diameter) are covalently attached to the silica nanoparticles by chemisorption forming a shell structure. Biotin is covalently bound to the gold shell surface by forming amide bonds and utilized for the detection of streptavidin with a sensitivity of 3.88 nm/(ng mm^{-2}) and a LOD of 0.86 pg mm^{-2}. Heidemann *et al.* have also prepared cysteamine-functionalized AuNPs on LPFG for online monitoring of glyphosate molecules, as shown in Fig. 33(c).[150] The LPFG operating near the dispersion turning point exhibits a highly sensitive wavelength shift, and the LOD of glyphosate in water is approximately 0.02 μM. Li *et al.* have theoretically investigated the excitation and sensing properties of the surface waveguide modes excited by gold–silica thin-film-coated LPFG, as shown in Fig. 33(d–f).[151] The surface waveguide modes originating from the intermode jumps of two neighboring EH cladding modes are produced by the surface silicon film, while the HE cladding modes remain stable. Highly sensitive refractive index sensing is accomplished by tracking the wavelength shift of the double resonance of the EH surface waveguide modes, with the insensitive HE cladding modes providing the additional advantage of self-referencing measurements. A high sensitivity of 7267.7 nm per RIU^{-1} is observed in the refractive index range of 1.315 to 1.335, which is 76 times higher than that of the bare LPFG sensor and 4 times higher than that of the common LPFG-SPR sensor. Although limited to theoretical investigation by numerical simulation, this study showcases the potential in highly sensitive biosensing (Table 3).

4. Perspectives and conclusion

In this review, recent advances in fibre-optic biosensors based on the phenomenon of surface plasmon resonance (SPR) are summarized. Various types of biosensors are categorized according to their structural features, with a focus on elucidating their sensing mechanisms, characteristics, fabrication, and applications. Primarily, in fields such as biomedical engineering, environmental monitoring, and clinical analysis, many optical fiber sensors exhibit superior properties compared to other detection techniques. Furthermore, SPR optical fiber biosensors hold extensive application prospects in precision medicine, immunosensing, biopharmaceuticals, environmental monitoring, and food safety. With the continuous development of nanotechnology, optics, and biochemistry, there is a growing demand for enhanced sensitivity, selectivity, and stability of SPR biosensors. Future directions include enhancing detection sensitivity, reducing costs, and enabling multi-channel detection. Additionally, optical fiber SPR biosensors are expected to achieve multifunctionality, enabling simultaneous detection of multiple biomolecules, thereby enhancing detection throughput, efficiency, and accuracy. Lastly, integrating optical fiber SPR biosensors with other sensing technologies, such as mass spectrometry and electrochemistry, can enable multimodal detection, enhancing comprehensive and accurate analysis. Recent experimental results confirm the vast application prospects of SPR optical fiber biosensors, albeit commercial products remain limited. Anticipated trends in the future development of SPR optical fiber biosensors will focus on streamlining manufacturing procedures, reducing production costs, identifying notable limitations, and meeting specific requirements.

Author contributions

The manuscript was written through contributions of all authors. All authors have approved the final version of the manuscript. Jingwei Lv: conceptualization, writing – original draft, writing – review & editing, funding acquisition. Jianxin Wang: investigation, writing – original draft, writing – review & editing. Lin Yang: investigation, writing – original draft. Wei Liu: conceptualization, writing – original draft. Haihao Fu: writing – review & editing, investigation. Paul K. Chu: writing – review & editing, funding acquisition. Chao Liu: conceptualization, supervision, writing – review & editing, funding acquisition.

Conflicts of interest

There are no conflicts to declare.

Acknowledgements

This work was jointly supported by the National Natural Science Foundation of China [12304480], Heilongjiang Provincial Natural Science Foundation of China [JQ2023F001], Local Universities Reformation and Development Personnel Training Supporting Project from Central Authorities, Natural Science Foundation of Heilongjiang Province [LH2021F007], China Postdoctoral Science Foundation funded project [2020M670881], Study Abroad returnees merit based Aid Foundation in Heilongjiang Province [070-719900103], City University of Hong Kong Strategic Research Grant (SRG) [7005505], and City University of Hong Kong Donation Research Grants [DON-RMG 9229021 and 9220061].

References

1 Q. Wang, D. Y. Zhang, Y. Z. Qian, X. Y. Yin, L. Wang, S. S. Zhang and Y. Y. Wang, *Photonic Sens.*, 2024, **14**, 240201.
2 Q. L. Duan, Y. N. Liu, S. S. Chang, H. Y. Chen and J. H. Chen, *Sensors*, 2021, **21**, 5262.
3 D. Capelli, V. Scognamiglio and R. Montanari, *TrAC, Trends Anal. Chem.*, 2023, **163**, 117079.
4 M. Chauhan, A. Pathak, T. Khanikar and V. Singh, *Workshop on Recent Advances in Photonics (WRAP)*, 2019, pp. 1–3.
5 S. Cai, H. Pan, Á. González-Vila, T. Guo, D. C. Gillan, R. Wattiez and C. Caucheteur, *Opt. Express*, 2020, **28**, 19740–19749.
6 X. Li, L. V. Nguyen, M. Becker, D. Pham, H. Ebendorff-Heidepriem and S. C. Warren-Smith, *IEEE J. Sel. Top. Quantum Electron.*, 2019, 1.
7 W. Zhou, K. Li, Y. Wei, P. Hao and M. Chi, *Biosens. Bioelectron.*, 2018, **106**, 99–104.
8 W. Zheng, B. Han, E. Siyu, Y. Sun, X. Li, Y. Cai and Y.-N. Zhang, *Microchem. J.*, 2020, **157**, 105010.
9 S. M. Chen, Y. Liu, Q. X. Yu and W. Peng, *J. Lightwave Technol.*, 2020, **38**, 2485–2492.
10 W. Luo, B. Liu, J. Liu, T. Wu, Q. Liu, M. Y. Wang, S. P. Wan, J. H. Yuan, P. Lu, D. L. Wang, X. D. He and Q. Wu, *IEEE Sens. J.*, 2022, **22**, 7727–7733.
11 Z. Y. Xiong, S. Gao, B. B. Li, Y. Liu, P. Li, J. Yang, J. H. Shi, L. B. Yuan and C. Y. Guan, *IEEE Photonics Technol. Lett.*, 2023, **35**, 1143–1146.
12 X. H. Fu, S. Y. Ma, R. J. Zhang, F. Liu, G. W. Fu, W. Jin and W. H. Bi, *IEEE Sens. J.*, 2021, **21**, 24098–24105.
13 L. Liu, Z. H. Liu, Y. Zhang and S. T. Liu, *IEEE Sens. J.*, 2021, **21**, 16621–16628.
14 Y. Wei, C. B. Liu, C. L. Liu, C. Shi, Z. Ren, Z. Ran, T. C. Jiang, R. Wang, X. K. Wang, Y. Zhang and Z. H. Liu, *IEEE Sens. J.*, 2022, **22**, 21719–21726.
15 V. S. Chaudhary, D. Kumar and S. Kumar, *IEEE Sens. J.*, 2021, **21**, 17800–17807.
16 V. S. Chaudhary, D. Kumar, B. P. Pandey and S. Kumar, *IEEE Sens. J.*, 2023, **23**, 1012–1023.
17 G. P. Mishra, D. Kumar, V. S. Chaudhary and S. Kumar, *IEEE Sens. J.*, 2022, **22**, 1265–1272.
18 Y. H. Ren, H. Song, Q. H. Cai, Z. J. Cai, Y. Liu and B. Y. Wang, *Opt. Fiber Technol.*, 2024, **84**, 103710.
19 L. Sun, T. Q. Liang, X. X. Sun, C. Li and C. W. Zhang, *Opt. Fiber Technol.*, 2023, **81**, 103539.
20 A. Uniyal, G. Srivastava, A. Pal, S. Taya and A. Muduli, *Plasmonics*, 2023, **18**, 735–750.
21 Y. Zhang, L. Zhou, D. Qiao, M. Liu, H. Yang, C. Meng, T. Miao, J. Xue and Y. Yao, *Micromachines*, 2022, **13**, 348.
22 S. C. Oostindie, G. A. Lazar, J. Schuurman and P. W. H. I. Parren, *Nat. Rev. Drug Discovery*, 2022, **21**, 715–735.
23 M. Loyez, M. Lobry, C. Caucheteur and R. Wattiez, *Optical Sensing and Detection VI*, 2020, vol. 11354, pp. 44–50.
24 S. Jhunjhunwala, C. Hammer and L. Delamarre, *Nat. Rev. Cancer*, 2021, **21**, 298–312.
25 G. Moro, F. Chiavaioli, S. Liberi, P. Zubiate, I. Del Villar, A. Angelini, K. De Wael, F. Baldini, L. M. Moretto and A. Giannetti, *Results Opt.*, 2021, **5**, 100123.
26 V. S. Chaudhary, D. Kumar and S. Kumar, *IEEE Trans. NanoBiosci.*, 2023, **22**, 562–569.
27 Z. Wang, R. Singh, C. Marques, R. Jha, B. Y. Zhang and S. Kumar, *Opt. Express*, 2021, **29**, 43793–43810.
28 Z. Cheng, Q. Wang, A. S. Zhu, F. M. Qiu, L. Y. Niu and J. Y. Jing, *Opt. Laser Technol.*, 2021, **134**, 106656.
29 Y. Z. Qian, Q. Wang, D. Y. Zhang, B. Li and H. Y. Wang, *Opt. Fiber Technol.*, 2023, **80**, 395–406.
30 X. Liu, A. L. Dang, T. H. Li, Y. T. Sun, T. C. Lee, W. B. Deng, S. H. Wu, A. Zada, T. K. Zhao and H. Li, *ACS Sens.*, 2023, **8**, 1287–1298.
31 A. Kohut, V. Horváth, Z. Pápa, B. Vajda, J. Kopniczky, G. Galbács and Z. Geretovszky, *Nanotechnology*, 2021, **32**, 395501.
32 A. M. Shrivastav, S. K. Mishra and B. D. Gupta, *Sens. Actuators, B*, 2015, **212**, 404–410.
33 H. Zhang, X. Li, X. Zhou, P. Gong and Y. Zhao, *Opt. Lett.*, 2023, **48**, 2138–2141.
34 E. Klantsataya, P. Jia, H. Ebendorff-Heidepriem, T. M. Monro and A. Franois, *Sensors*, 2017, **17**, 12.
35 H. Y. Lin, C. H. Huang, G. L. Cheng, N. K. Chen and H. C. Chui, *Opt. Express*, 2012, **20**, 21693–21701.

36 Q. Wang, J. Y. Jing and B. T. Wang, *IEEE Trans. Instrum. Meas.*, 2018, **68**, 3350–3357.
37 S. Y. Qian, Y. Zhang, H. Z. Yuan, W. Ji, Y. Liu, J. Z. Zhao, M. Han and W. Peng, *Sens. Actuators, B*, 2018, **260**, 976–982.
38 Y. Liu, P. Li, N. Zhang, S. M. Chen, Z. G. Liu and J. Y. Guang, *IEEE Sens. J.*, 2019, **19**, 11955–11960.
39 Y. Hua, R. D. Wang and D. C. Li, *Micromachines*, 2022, **13**, 1036.
40 D. Daems, W. Pfeifer, I. Rutten, B. Saccà, D. Spasic and J. Lammertyn, *ACS Appl. Mater. Interfaces*, 2018, **10**, 23539–23547.
41 C. Desmet, K. Vindas, R. Alvarado Meza, P. Garrigue, S. Voci, N. Sojic, A. Maziz, R. Courson, L. Malaquin, T. Leichle, A. Buhot, Y. Roupioz, L. Leroy and E. Engel, *Sensors*, 2020, **20**, 511, DOI: 10.21203/rs.3.rs-684898/v1.
42 Y. F. Duan, Y. Zhang, F. Wang, Y. T. Sun, M. Chen, Z. G. Jing, Q. Wang, M. D. Lu and W. Peng, *Photonic Sens.*, 2022, **12**, 23–30.
43 Y. F. Chen, S. H. Peng, P. L. Zhao, L. Chen, G. S. Liu, D. Y. Ouyang, Y. H. Luo and Z. Chen, *Biomed. Opt. Express*, 2022, **13**, 274–283.
44 W. Gong, S. Z. Jiang, Z. Li, C. H. Li, J. H. Xu, J. Pan, Y. Y. Huo, B. Y. Man, A. H. Liu and C. Zhang, *Opt. Express*, 2019, **27**, 3483–3495.
45 B. B. Luo, Y. F. Xu, S. X. Wu, M. F. Zhao, P. J. Jiang, S. H. Shi, Z. H. Zhang, Y. Wang, L. L. Wang and Y. Liu, *Biosens. Bioelectron.*, 2018, **100**, 169–175.
46 B. Lee, *Biosens. Bioelectron.*, 2018, **102**, 504–509.
47 A. Otto, *Z. Phys.*, 1968, **216**, 398–410.
48 E. Kretschmann and H. Raether, *Z. Naturforsch., A: Astrophys., Phys. Phys. Chem.*, 1968, **23**, 2135–2136.
49 R. H. Ritchie, *Phys. Rev.*, 1957, **106**, 874.
50 H. Raether, *Surface Plasmons on Smooth and Rough Surfaces and on Gratings*, Springer Tracts in Modern Physics, 1988, vol. 111, pp. 1–133.
51 C. Liu, J. Lü, W. Liu, F. Wang and P. K. Chu, *Chin. Opt. Lett.*, 2021, **19**, 102202.
52 R. C. Jorgenson and S. S. Yee, *Sens. Actuators, B*, 1993, **12**, 213–220.
53 R. Kant, R. Tabassum and B. D. Gupta, *IEEE Photonics Technol. Lett.*, 2016, **28**, 2050–2053.
54 A. Pathak, *ACS Appl. Nano Mater.*, 2020, **3**, 2582–2593.
55 S. Kaushik, U. K. Tiwari, S. S. Pal and R. K. Sinha, *Biosens. Bioelectron.*, 2019, **126**, 501–509.
56 M. Hossain, S. Muktadhir and M. M. Rana, *Optik*, 2016, **127**, 5841–5851.
57 M. B. Hossain, M. M. Islam, L. F. Abdulrazak, M. M. Rana, T. B. A. Akib and M. Hassan, *Photonic Sens.*, 2020, **10**, 67–79.
58 M. Lu, H. Zhu, M. Lin, F. Wang, L. Hong, J.-F. Masson and W. Peng, *Sens. Actuators, B*, 2021, **329**, 129094.
59 A. Dillen, C. Scarpellini, W. Daenen, S. Driesen, P. Zijlstra and J. Lammertyn, *ACS Sens.*, 2023, **8**, 811–821.
60 A. Hosoki, M. Nishiyama, H. Igawa, A. Seki, Y. Choi and K. Watanabe, *Sens. Actuators, B*, 2013, **185**, 53–58.
61 Z. Zhu, L. Liu, Z. Liu, Y. Zhang and Y. Zhang, *Opt. Lett.*, 2017, **42**, 1982–1985.
62 Q. Wang and B. Wang, *Optics & Laser Technology*, 2018, **107**, 210–215.
63 S. Kumar, Z. Guo, R. Singh, Q. Wang, B. Zhang, S. Cheng, F.-Z. Liu, C. Marques, B. K. Kaushik and R. Jha, *J. Lightwave Technol.*, 2021, **39**, 4069–4081.
64 M. H. Chiu, S. N. Hsu and H. Yang, *Sens. Actuators, B*, 2004, **101**, 322–327.
65 H.-Y. Lin, W.-H. Tsai, Y.-C. Tsao and B.-C. Sheu, *Appl. Opt.*, 2007, **46**, 800–806.
66 B. Du, Y. Yang, Y. Zhang and D. Yang, *Plasmonics*, 2019, **14**, 457–463.
67 N. Cennamo, L. Pasquardini, F. Arcadio, L. E. Vanzetti, A. M. Bossi and L. Zeni, *Sci. Rep.*, 2019, **9**, 18740.
68 X. Xi, J. Xu, S. Li, J. Song, W. Yang, Y. Sun, S. Jiang, Y. Han and X. Fan, *Sensors*, 2020, **20**, 991.
69 R. Zakaria, N. Zainuddin, M. A. Fahri, A. Kamkar, F. A. Al Zahrani, S. K. Patel and K. Ahmed, *Opt. Quantum Electron.*, 2021, DOI: 10.21203/rs.3.rs-684898/v1.
70 S. Lyu, Z. Wu, X. Shi and Q. Wu, *Appl. Opt.*, 2022, **58**, 4149–4156.
71 L. Zeni, N. Cennamo, M. Pesavento and G. D'Agostino, *Sens. Actuators, B*, 2014, **191**, 529–536.
72 A. Urrutia, K. Bojan, L. Marques, K. Mullaney, J. Goicoechea, S. James, M. Clark, R. Tatam and S. Korposh, *J. Sens.*, 2016, **2016**, 8129387.
73 P. K. Maharana, P. Padhy and R. Jha, *IEEE Photonics Technol. Lett.*, 2013, **25**, 2156–2159.
74 H. W. Liu, Y. X. Sun, J. Guo, W. Liu, L. Liu, Y. Meng and X. Yu, *IEEE Access*, 2021, **9**, 116286–116293.
75 W. J. Wang, Z. G. Mai, Y. Z. Chen, J. Q. Wang, L. Li, Q. N. Su, X. J. Li and X. M. Hong, *Sci. Rep.*, 2017, **7**, 16904.
76 Y. Yanase, A. Araki, H. Suzuki, T. Tsutsui, T. Kimura, K. Okamoto, T. Nakatani, T. Hiragun and M. Hide, *Biosens. Bioelectron.*, 2010, **25**, 1244–1247.
77 Q. Wang and B. T. Wang, *Sens. Actuators, B*, 2018, **275**, 332–338.
78 S. Kumar, R. Singh, G. Zhu, Q. S. Yang, X. Zhang, S. Cheng, B. Y. Zhang, B. K. Kaushik and F. Z. Liu, *IEEE Trans. NanoBiosci.*, 2020, **19**, 173–182.
79 S. Kaushik, U. K. Tiwari, S. S. Pal and R. K. Sinha, *Biosens. Bioelectron.*, 2019, **126**, 501–509.
80 Q. Wang, B. Sun, E. Hu and W. Wei, *IEEE Photonics Technol. Lett.*, 2019, **31**, 1159–1162.
81 K. N. Shushama, M. M. Rana, R. Inum and M. B. Hossain, *Opt. Commun.*, 2017, **383**, 186–190.
82 M. S. Rahman, M. S. Anower, M. K. Rahman, M. R. Hasan, M. B. Hossain and M. I. Haque, *Optik*, 2017, **140**, 989–997.
83 K. Liu, J. H. Zhang, J. F. Jiang, T. H. Xu, S. Wang, P. X. Chang, Z. Zhang, J. Y. Ma and T. G. Liu, *IEEE Access*, 2020, **8**, 660–668.
84 L. Pasquardini, N. Cennamo, G. Malleo, L. Vanzetti, L. Zeni, D. Bonamini, R. Salvia, C. Bassi and A. M. Bossi, *Sensors*, 2021, **21**, 3443.

85 R. Kant and B. D. Gupta, *J. Lightwave Technol.*, 2018, **36**, 4018–4024.

86 H. S. Jang, K. N. Park, C. D. Kang, J. P. Kim, S. J. Sim and K. S. Lee, *Opt. Commun.*, 2009, **282**, 2827–2830.

87 M. S. Rahman, M. S. Anower and L. F. Abdulrazak, *Results Phys.*, 2019, **15**, 102623.

88 T. T. Nguyen, K. T. L. Trinh, W. J. Yoon, N. Y. Lee and H. Ju, *Sens. Actuators, B*, 2017, **242**, 1–8.

89 W. Liu, Y. Shi, Z. Yi, C. Liu, F. M. Wang, X. L. Li, J. W. Lv, L. Yang and P. K. Chu, *Opt. Express*, 2021, **29**, 40734–40747.

90 H. X. Han, D. L. Hou, L. Zhao, N. N. Luan, L. Song, Z. H. Liu, Y. D. Lian, J. F. Liu and Y. S. Hu, *Sensors*, 2020, **20**, 1009.

91 C. G. Li, B. Yan and J. J. Liu, *J. Opt. Soc. Am. A*, 2019, **36**, 1663–1668.

92 M. S. Hossain, M. M. Hasan, S. Sen, M. S. H. Mollah and M. M. Azad, *J. Opt. Commun.*, 2021, **44**, s631–s639.

93 G. Liang, Z. Luo, K. Liu, Y. Wang and Y. Duan, *Crit. Rev. Anal. Chem.*, 2016, **46**, 213–223.

94 H. X. Yu, Y. Chong, P. H. Zhang, J. M. Ma and D. C. Li, *Talanta*, 2020, **219**, 121324.

95 P. Q. Gong, Y. M. Wang, X. Zhou, S. K. Wang, Y. A. Zhang, Y. Zhao, L. V. Nguyen, H. Ebendorff-Heidepriem, L. Peng, S. C. Warren-Smith and X. G. Li, *Anal. Chem.*, 2021, **93**, 10561–10567.

96 D. Li, D. Yang, J. Yang, Y. Lin, Y. Sun, H. Yu and K. Xu, *Sens. Actuators, A*, 2015, **222**, 58–66.

97 W. Nie, Q. Wang, L. Zou, Y. Zheng, X. Liu, X. Yang and K. Wang, *Anal. Chem.*, 2018, 12584–12591.

98 M. Abdelghaffar, Y. Gamal, R. A. El-Khoribi and W. Soliman, *Opt. Quantum Electron.*, 2023, **55**, 472.

99 M. A. Mollah, M. Yousufali, I. M. Ankan, M. M. Rahman, H. Sarker and K. Chakrabarti, *Sens. Bio-Sens. Res.*, 2020, **29**, 100344.

100 M. Fazeli and A. Horri, *Research Square*, 2021, preprint, DOI: **10.21203/rs.3.rs-397327/v1**.

101 M. M. A. Eid, A. M. Bulbul, E. Podder and A. N. Z. Rashed, *Plasmonics*, 2020, **3**, 717–727.

102 A. Natesan, K. P. Govindasamy, T. R. Gopall, V. Dhasarathan and A. H. Aly, *IET Optoelectron.*, 2019, **13**, 118–123.

103 A. Yaşlı and H. Ademgil, Modeling the Photonic Crystal Fiber based Surface Plazmon Resonance Biosensor to Detect Blood Components, in *2021 29th Signal Processing and Communications Applications Conference (SIU)*, IEEE, 2021, pp. 1–4.

104 F. Xia, H. Song, Y. Zhao, W.-M. Zhao, Q. Wang, X.-Z. Wang, B.-T. Wang and Z.-X. Dai, *Measurement*, 2020, **164**, 108083.

105 J. Roether, K. Y. Chu, N. Willenbacher, A. Q. Shen and N. Bhalla, *Biosens. Bioelectron.*, 2019, **142**, 111528.

106 Z. Ailing, L. I. Yueting, P. Fei, P. Honggang and L. Fei, *Optoelectron. Lett.*, 2022, **18**, 0204–0209.

107 M. Liu, X. Leng, W. Ni and P. P. Shum, *Plasmonics*, 2023, 1–11.

108 J. Divya and S. Selvendran, *Biosensors*, 2023, **13**, 148.

109 W. Zhang, Z. Lian, T. M. Benson, X. Wang and S. Lou, *J. Opt.*, 2019, **21**, 025001.

110 A. D. Kersey, M. A. Davis, H. J. Patrick, M. LeBlanc, K. P. Koo, C. G. Askins, M. A. Putnam and E. J. Friebele, *J. Lightwave Technol.*, 1997, **15**, 1442–1463.

111 G. Nemova and R. Kashyap, *Opt. Lett.*, 2006, **31**, 2118–2120.

112 J. Sun, C. C. Chan, Y. F. Zhang and P. Shum, *J. Biomed. Opt.*, 2008, **13**, 054048.

113 N. Jahan, M. M. Rahman, M. Ahsan, M. A. Based, M. M. Rana, S. Gurusamy and J. Haider, *IEEE Access*, 2021, **9**, 42206–42215.

114 S. Jain, K. Choudhary and S. Kumar, *Opt. Fiber Technol.*, 2022, **73**, 103030.

115 M. Li, R. Singh, M. S. Soares, C. Marques, B. Zhang and S. Kumar, *Opt. Express*, 2022, **30**, 13898–13914.

116 E. Coscelli, M. Sozzi, F. Poli, D. Passaro, A. Cucinotta, S. Selleri, R. Corradini and R. Marchelli, *IEEE J. Sel. Top. Quantum Electron.*, 2010, **16**, 967–972.

117 M. R. Hasan, S. Akter, A. A. Rifat, S. Rana, K. Ahmed, R. Ahmed, H. Subbaraman and D. Abbott, *IEEE Sens. J.*, 2017, **18**, 133–140.

118 D. Rajeswari and A. A. Revathi, *Optik*, 2022, **258**, 168897.

119 R. Srivastava, Y. K. Prajapati, S. Pal and S. Kumar, *IEEE Sens. J.*, 2022, **22**, 14834–14841.

120 F. Abdelmalek, *Mater. Lett.*, 2002, **57**, 213–218.

121 B. Špačková and J. Homola, *Opt. Express*, 2009, **17**, 23254–23264.

122 P. T. Arasu, Y. Al-Qazwini and B. I. Onn, *et al.*, Fiber Bragg grating based surface plasmon resonance sensor utilizing FDTD for alcohol detection applications, *2012 IEEE 3rd International Conference on Photonics*, IEEE, 2012, pp. 93–97.

123 J. Burgmeier, A. Feizpour, W. Schade and B. M. Reinhard, *Opt. Lett.*, 2015, **40**, 546–549.

124 A. Bekmurzayeva, K. Dukenbayev, M. Shaimerdenova, I. Bekniyazov, T. Ayupova, M. Sypabekova, C. Molardi and D. Tosi, *Sensors*, 2018, **18**, 4298.

125 K. Chah, V. Voisin, D. Kinet and C. Caucheteur, *Opt. Lett.*, 2014, **39**, 6887–6890.

126 A. Candiani, A. Bertucci, S. Giannetti, M. Konstantaki, A. Manicardi, S. Pissadakis, A. Cucinotta, R. Corradini and S. Selleri, *J. Biomed. Opt.*, 2013, **18**, 057004–057004.

127 P. Arasu, A. Noor, A. Shabaneh, M. Yaacob, H. Lim and M. Mahdi, *Opt. Commun.*, 2016, **380**, 260–266.

128 O. Rusyakina, T. Baghdasaryan, K. Chah, P. Mergo, H. Thienpont, C. Caucheteur, F. Berghmans and T. Geernaert, *J. Lightwave Technol.*, 2021, **40**, 1121–1129.

129 Y. Y. Shevchenko and J. Albert, *Opt. Lett.*, 2007, **32**, 211–213.

130 Y. Shevchenko, C. Chen, M. Dakka and J. Albert, *Opt. Lett.*, 2010, **35**, 637–639.

131 Y. Shevchenko, T. J. Francis, D. A. Blair, R. Walsh, M. C. DeRosa and J. Albert, *Anal. Chem.*, 2011, **83**, 7027–7034.

132 Y. Shevchenko, G. Camci-Unal, D. F. Cuttica, M. R. Dokmeci, J. Albert and A. Khademhosseini, *Biosens. Bioelectron.*, 2014, **56**, 359–367.

133 V. Malachovska, C. Ribaut, V. Voisin, M. Surin, P. Leclere, R. Wattiez and C. Caucheteur, *Anal. Chem.*, 2015, **87**, 5957–5965.

134 V. Voisin, J. Pilate, P. Damman, P. Mégret and C. Caucheteur, *Biosens. Bioelectron.*, 2014, **51**, 249–254.

135 T. Guo, F. Liu, X. Liang, X. Qiu, Y. Huang, C. Xie, P. Xu, W. Mao, B.-O. Guan and J. Albert, *Biosens. Bioelectron.*, 2016, **78**, 221–228.

136 C. Ribaut, M. Loyez, J. C. Larrieu, S. Chevineau, P. Lambert, M. Remmelink, R. Wattiez and C. Caucheteur, *Biosens. Bioelectron.*, 2017, **92**, 449–456.

137 X. Zhang, Z. Wu, F. Liu, Q. Fu, X. Chen, J. Xu, Z. Zhang, Y. Huang, Y. Tang and T. Guo, *Biomed. Opt. Express*, 2018, **9**, 1735–1744.

138 A. González-Vila, A. Ioannou, M. Loyez, M. Debliquy, D. Lahem and C. Caucheteur, *Opt. Lett.*, 2018, **43**, 2308–2311.

139 F. Wang, Y. Zhang, M. D. Lu, Y. T. Du, M. Chen, S. Meng, W. Ji, C. S. Sun and W. Peng, *Sens. Actuators, B*, 2021, **337**, 129816.

140 H. Qu, L. Tan, F.-C. Wu, W. Huang, K. Li, X. Chen, Y.-W. Xu and X. Hu, *Biomed. Opt. Express*, 2023, **14**, 5921–5931.

141 C. Y. Shen, Z. L. Huang, X. M. Chen, Z. H. Wang, J. Zhou, Z. K. Wang, D. J. Liu, C. X. Li, T. Q. Zhao, Y. Zhang, S. Q. Xu, W. J. Zhou and W. Peng, *Biosens. Bioelectron.*, 2023, **242**, 115719.

142 H. J. Patrick, A. D. Kersey and F. Bucholtz, *J. Lightwave Technol.*, 1998, **16**, 1606–1612.

143 Y. J. He, Y. L. Lo and J. F. Huang, *J. Opt. Soc. Am. B*, 2006, **23**, 801–811.

144 Y. J. He, *Opt. Express*, 2013, **21**, 13875–13895.

145 J. L. Tang, S. F. Cheng, W. T. Hsu, T. Y. Chiang and L. K. Chau, *Sens. Actuators, B*, 2006, **119**, 105–109.

146 R. Kumar, Y. K. Leng, B. Liu, J. Zhou, L. Y. Shao, J. H. Yuan, X. Y. Fan, S. P. Wan, T. Wu, J. Liu, R. Binns, Y. Q. Fu, W. P. Ng, G. Farrell, Y. Semenova, H. Y. Xu, Y. H. Xiong, X. D. He and Q. Wu, *Biosens. Bioelectron.*, 2019, **145**, 111563.

147 L. Marques, F. U. Hernandez, S. W. James, S. P. Morgan, M. Clark, R. P. Tatam and S. Korposh, *Biosens. Bioelectron.*, 2016, **75**, 222–231.

148 W. Wei, J. Nong, G. Zhang, L. Tang, X. Jiang, N. Chen, S. Luo, G. Lan and Y. Zhu, *Sensors*, 2016, **17**, 2.

149 L. L. Liu, L. Marques, R. Correia, S. P. Morgan, S. W. Lee, P. Tighe, L. Fairclough and S. Korposh, *Sens. Actuators, B*, 2018, **271**, 24–32.

150 B. R. Heidemann, I. Chiamenti, M. M. Oliveira, M. Muller and J. L. Fabris, *J. Lightwave Technol.*, 2018, **36**, 863–870.

151 Z. Li and H. Zhu, *Opt. Lett.*, 2021, **46**, 266–269.